Clim. Past, 16, 1523–1545, 2020
https://doi.org/10.5194/cp-16-1523-2020

Climate of the Past
Open Access
EGU

Pliocene Model Intercomparison Project (PlioMIP2) simulations using the Model for Interdisciplinary Research on Climate (MIROC4m)

Wing-Le Chan[1] **and Ayako Abe-Ouchi**[1,2]

[1]Atmosphere and Ocean Research Institute, The University of Tokyo, Kashiwa, 277-8564, Japan
[2]National Institute for Polar Research, Tachikawa, 190-8518, Japan

Correspondence: Wing-Le Chan (wlchan@aori.u-tokyo.ac.jp)

Received: 7 February 2020 – Discussion started: 19 February 2020
Revised: 25 May 2020 – Accepted: 2 July 2020 – Published: 17 August 2020

Abstract. The second phase of the Pliocene Model Intercomparison Project (PlioMIP2) has attracted many climate modelling groups in its continuing efforts to better understand the climate of the mid-Piacenzian warm period (mPWP) when atmospheric CO_2 was last closest to present-day levels. Like the first phase, PlioMIP1, it is an internationally coordinated initiative that allows for a systematic comparison of various models in a similar manner to the Paleoclimate Modelling Intercomparison Project (PMIP). Model intercomparison and model–data comparison now focus specifically on the interglacial at marine isotope stage KM5c (3.205 Ma), and experimental design is not only based on new boundary conditions but includes various sensitivity experiments. In this study, we present results from long-term model integrations using the MIROC4m (Model for Interdisciplinary Research on Climate) atmosphere–ocean coupled general circulation model, developed at the institutes CCSR, NIES and FRCGC in Japan. The core experiment, with CO_2 levels set to 400 ppm, shows a warming of 3.1 °C compared to the pre-industrial period, with two-thirds of the warming being attributed to the increase in CO_2. Although this level of warming is less than that in the equivalent PlioMIP1 experiment, there is slightly better agreement with proxy sea surface temperature (SST) data at PRISM3 (PRISM – Pliocene Research Interpretation and Synoptic Mapping) locations, especially in the northern North Atlantic where there were large model–data discrepancies in PlioMIP1. Similar spatial changes in precipitation and sea ice are seen and the Arctic remains ice-free in the summer in the core experiments of both phases. Comparisons with both the proxy SST data and proxy surface air temperature data from paleobotanical sites indicate a weaker polar amplification in model results. Unlike PlioMIP1, the Atlantic Meridional Overturning Circulation (AMOC) is now stronger than that of the pre-industrial period, even though increasing CO_2 tends to weaken it. This stronger AMOC is a consequence of a closed Bering Strait in the PlioMIP2 paleogeography. Also, when present-day boundary conditions are replaced by those of the Pliocene, the dependency of the AMOC strength on CO_2 is significantly weakened. Sensitivity tests show that lower values of CO_2 give a global SST which is overall more consistent with the PRISM3 SST field presented in PlioMIP1, while SSTs at many of the PRISM4 sites are still too high to be reconciled with any of the model results. On the other hand, tropical Pacific SST in the core experiment agrees well with more recent proxy data, which suggested that PRISM3 SST there was overestimated. Future availability of climate reconstructions from proxy data will continue to help evaluate model results. The inclusion of dynamical vegetation and the effects of all possible extreme orbital configurations outside KM5c should be considered in future experiments using MIROC4m for the mPWP.

1 Introduction

The mid-Pliocene was the most recent period in the Earth's history to have experienced sustained levels of atmospheric CO_2 similar to those of the present day. Global temperatures are also estimated to have been 2–3 °C higher than those of the present day (Chandler et al., 2008). Various kinds

of proxy evidence, including pollen assemblages (Brigham-Grette et al., 2013) and tetraether lipids (Crampton-Flood, 2018), have been used to reconstruct larger temperature changes at northern high latitudes. As a clear understanding of climate change in the near future becomes ever more important, scientists have also looked to warm climates of the past to validate model predictions and to quantify the forcings responsible for large climatic shifts. The mid-Pliocene has often been thought of as a good analogue for near-future climates, with formal assessments based on quantitative comparisons between past warm periods and Representative Concentration Pathway emission scenarios (Burke et al., 2018). The first studies of the mid-Pliocene using climate models were those of Chandler et al. (1994), whose results using the GISS atmospheric general circulation model (AGCM) showed a decrease in the Equator-to-pole temperature gradient, and of Sloan et al. (1996), who found a global surface temperature increase of 3.6 °C with the NCAR GENESIS AGCM. These were eventually followed by studies using coupled atmosphere–ocean models, such as HadCM3 (Haywood and Valdes, 2004; Lunt et al., 2008) and NCAR CCMS3 (Jochum et al., 2009). Some of these studies investigated the specific effects of changing seaways and mountain uplifts which occurred during that time. Simultaneously, there have been ongoing efforts with reconstructions of the mid-Pliocene climate using a multitude of marine and terrestrial proxy data. PRISM (Pliocene Research Interpretation and Synoptic Mapping) reconstructions of sea surface temperature (SST) and vegetation were first introduced in Dowsett et al. (1994) and are still ongoing. Pollen assemblages from marine sediments have been used in Panitz et al. (2016) to reconstruct fluctuations of cool temperate and boreal conditions in northern Norway between 3.6 and 3.14 Ma. Plant macrofossils preserved in sediments across the Canadian Arctic Archipelago (Fletcher et al., 2017) have shown warmer and wetter conditions up to the mid-Pliocene in that region.

The Pliocene Model Intercomparison Project (PlioMIP) was initiated at a time when climate models were increasingly used to simulate past climates to assess their performances by way of model intercomparison or model–data comparison (e.g. Braconnot et al., 2007). The first phase (Haywood et al., 2010, 2011), henceforth named PlioMIP1, focused on the mid-Piacenzian warm period (mPWP) within the mid-Pliocene, defined by PRISM as the interval between 3.264 and 3.025 Ma. Adhering to the experimental designs specified in PlioMIP1 and using PRISM3D boundary conditions, models simulated an annual mean surface temperature increase of 1.8 to 3.6 °C from pre-industrial values, in addition to the aforementioned decrease in the Equator-to-pole temperature gradient (Haywood et al., 2013). Despite this polar amplification, models were unable to replicate the scale of warming in the northern North Atlantic as suggested by PRISM3 proxy data (Dowsett et al., 2013). Subsequent model intercomparison studies yielded findings on the intensification of the East Asian monsoon during the mPWP (R. Zhang et al., 2013), the different responses of the Atlantic Meridional Overturning Circulation (Z. Zhang et al., 2013) and the importance of albedo feedbacks to high-latitude warming (Hill et al., 2014), amongst other topics.

Lessons learnt and new insights gained from PlioMIP1 were applied to the second phase of the project, PlioMIP2 (Haywood et al., 2016), and an attempt was made to address shortcomings from the design in the first phase, namely, uncertainties in the boundary conditions, data and model physics, which could contribute to model–data discord. New reconstructions for paleogeography, land surface elevation and ice sheet distribution as part of PRISM4 were used as boundary conditions for PlioMIP2 experiments (Dowsett et al., 2016), including the closure of the Bering Strait and a smaller Greenland ice sheet restricted to the eastern part of the island. As opposed to a time slab or interval, the reconstructions now focus on a particular time slice, the interglacial peak, Marine Isotope Stage KM5c (3.205 Ma), which has an orbital forcing close to that of the present day. Additionally, PlioMIP2 forms part of the fourth phase of the Paleoclimate Modelling Intercomparison Project (PMIP4) and the sixth phase of the Coupled Model Intercomparison Project (CMIP6) (Kageyama et al., 2018).

PlioMIP2 also laid out plans for non-core sensitivity experiments to investigate the effects of individual boundary conditions and to account for the uncertainty in greenhouse gas levels. Estimates of CO_2 for this period from different marine proxy records vary widely, from 250 to 450 ppm (Fedorov et al., 2013), including uncertainties in individual sources. Values in the upper half of that range are inferred from alkenone-derived $\delta^{13}C$ and foraminiferal $\delta^{11}B$ (Seki et al., 2010; Martínez-Botí et al., 2015), stomatal properties of leaves (Kürschner et al., 1996), and marine plankton $\delta^{13}C$ (Raymo et al., 1996). Estimates from the lower half are derived from B/Ca ratios in foraminifera (Tripati et al., 2009) and other foraminiferal $\delta^{11}B$ (Bartoli et al., 2011). The core experiment in PlioMIP2 has a setting of 400 ppm for CO_2, which accounts for greenhouse gas forcing from all sources and is close to the PlioMIP1 value.

The main aim of this study is to present results of both core and some non-core PlioMIP2 experiments using MIROC4m (Model for Interdisciplinary Research on Climate). With these results, we investigate the differences in the climate state when switching from PlioMIP1 boundary conditions to PlioMIP2. Using results from non-core experiments, we examine the individual effects of increasing CO_2 and of introducing PlioMIP2 boundary conditions. We also compare proxy data with our model results, including those from sensitivity experiments using a range of CO_2 levels.

2 Model description

In the present study, the experiments have been carried out with the coupled atmosphere–ocean general circulation model, MIROC4m, a mid-resolution model developed jointly by the Center for Climate System Research (CCSR), National Institute for Environmental Studies (NIES) and Frontier Research Center for Global Change (FRCGC), in Japan (K-1 model developers, 2004). This model has previously been used to study a variety of climate states, for example, future RCP4.5 and RCP8.5 scenarios (Bakker et al., 2016), the mid-Holocene (Ohgaito et al., 2013), the Last Glacial Maximum (Yanase and Abe-Ouchi, 2007), and the mPWP (Chan et al., 2011). The same model with a higher resolution was included in the Fifth Assessment Report of the Intergovernmental Panel on Climate Change (IPCC, 2013). Note that this model is not a contributing member to PMIP4/CMIP6, and so results in this study are confined to PlioMIP2.

The model consists of an atmosphere–land–river component and a sea-ice–ocean component, with the air–sea exchange of momentum, heat and water occurring at the air–sea ice interface. At ice-free grid cells, exchange still occurs via the sea ice subcomponent but the flux to the ocean remains unaffected by the sea ice. Below is a brief description and readers should refer to K-1 model developers (2004) and the references contained within for further details.

The atmospheric component is identical to the AGCM described in Numaguti et al. (1997), namely, CCSR–NIES–FRCGC AGCM5.7b. The horizontal resolution is set to T42, which corresponds to a grid size of approximately 2.8° longitude and latitude and the number of levels is set to 20 in the σ coordinate system where pressure at all heights is scaled with the surface pressure. The U.S. Geological Survey's Global 30 Arc-Second Elevation (USGS GTOPO30) is used to generate the surface elevation. The level 2 scheme of the turbulence closure model by Mellor and Yamada (1982) is used for sub-grid vertical fluxes of prognostic variables. A radiative transfer scheme (Nakajima et al., 2000) based on the two-stream discrete ordinate and k-distribution methods is employed. Other physical parameterisations include a prognostic Arakawa–Schubert cumulus scheme and a prognostic cloud water scheme for large-scale condensation (Le Trent and Li, 1991). Optical parameters for water cloud, ice cloud and five aerosol types – soil dust, black carbon, organic carbon, sulfate and sea salt – are included. Classification of aerosols is based on Spectral Radiation-Transport Model for Aerosol Species (SPRINTARS) (Takemura et al., 2000). Indirect effects of aerosols are considered for condensation in stratus clouds. Monthly aerosol mass and particle number concentration used in radiative processes are prescribed offline by SPRINTARS.

The land surface model used is Minimal Advanced Treatments of Surface Interaction and Runoff (MATSIRO) (Takata et al., 2003), whose horizontal resolution is the same as that of the atmospheric component. Here, water and heat exchange between the land surface and atmosphere is computed. Within the same model, runoff on the land is also calculated and passed over to a river routing model which transports the runoff water to the ocean model at river mouths. Prognostic variables include canopy water content, canopy temperature and soil moisture. Land-cover classification is derived from USGS GLCC (Global Land Cover Characterization). See Chan et al. (2011) for the present-day vegetation distribution.

The ocean component is basically version 3.4 of the CCSR Ocean Component Model (COCO) (Hasumi, 2000). The horizontal grid has 256×192 points so that each grid point is spaced equally at 1.40625° in the longitudinal direction. In the latitudinal direction, resolution is highest in the tropics (0.56°) and lowest at the polar regions (1.4°). The are 43 vertical levels, including 8σ levels near the sea surface. Here, σ denotes a normalised geopotential height, with a value of 1 at the free surface and 0 at a fixed depth above which the σ coordinate system is applied. The Bering Strait throughflow is fully represented, but the Hudson Bay and the Mediterranean Sea are treated as isolated lakes with heat and salinity exchanged with the open seas by a two-way linear damping. A simple, vertical adjustment is applied, whereby unstable water columns are homogenised instantaneously. Vertical mixing of sea tracers and momentum use viscosity and diffusion coefficients calculated by Noh and Kim (1999). While there are no changes to the model as used in PlioMIP1, it should be noted that a larger Gent–McWilliams coefficient has been used in other more recent published work using MIROC4m (Obase and Abe-Ouchi, 2019; Sherriff-Tadano and Abe-Ouchi, 2020). This coefficient, which refers to the horizontal diffusion of the isopycnal layer thickness, is set to $300\ m^2\ s^{-1}$ in the present study.

Sea ice concentration, thickness and horizontal velocities are calculated in the sea ice model. The equation of momentum includes an advection term, a Coriolis term, an acceleration term due to the slope of the sea surface, an internal stress term, and an external forcing term derived from wind stress and ice–ocean drag. Upward longwave radiative flux is calculated according to the Stefan–Boltzmann law with an emissivity of 0.95. The albedo of bare ice surface is set to a constant value of 0.5, and that of snow-covered surface varies between 0.65 and 0.85, depending on the temperature. The air–sea and air–sea-ice flux is calculated by taking into account downward shortwave and longwave radiative fluxes calculated in the atmospheric model.

3 Experimental design

The nomenclature used for the experiments follows that specified for PlioMIP2 (Haywood et al., 2016); that is, it takes the form Ex^c, where c is the concentration of CO_2 in ppm and x can be any combination of the Pliocene boundary conditions. With present-day boundary conditions only, x is

null; otherwise it can be o (Pliocene orography, bathymetry, land–sea mask, lakes and soils combined) and/or i (Pliocene ice sheets).

Altogether, results from eight experiments are included in this study. Firstly, there are the two core experiments, the pre-industrial (E^{280}) and a Pliocene time slice (Eoi^{400}), which all modelling groups participating in PlioMIP2 are expected to run. Secondly, with the pre-industrial set-up, atmospheric CO_2 levels are increased to 400 ppm and double that of the pre-industrial period (E^{400} and E^{560}). Thirdly, at the Pliocene time slice, atmospheric CO_2 levels are changed to 280, 350 and 450 ppm (Eoi^{280}, Eoi^{350} and Eoi^{450}). These two groups form part of the Tier 1 and 2 experiments. Fourthly, we include an experiment with all boundary conditions set to those of the mPWP in PlioMIP1 and name this Eplio1 as it is not formally part of PlioMIP2. In the core, pre-industrial experiment, atmospheric CO_2, CH_4 and N_2O levels were initially set to those used for the MIROC4m experiments in PlioMIP1 (see Chan et al., 2011) for consistency, and these levels differed slightly from the specifications set in PlioMIP2. All the other experiments in this study subsequently followed the pre-industrial period, including the double CO_2 experiment, in which CO_2 is set to approximately 571 ppm. In order that MIROC4m results may be compared systematically with data from other modelling groups in future studies, the eight experiments are continued for a further 1000 model years with the three greenhouse gas levels set to those specified in Haywood et al. (2016). Final CO_2 levels and boundary conditions for each experiment are listed in Table 1. Common to all experiments are the other greenhouse gases, astronomical parameters and the solar constant which are listed in Table 2.

3.1 Pre-industrial (E^{280}) and increased CO_2 experiments (E^{400} and E^{560})

These three experiments with present-day land topography were run previous to this study. The CO_2 level for the pre-industrial (E^{280}) is initially set to 285.431 ppm, in accordance with previous MIROC4m experiments, and thus double the pre-industrial level is set to 570.862 ppm. The model was integrated for 1220, 2000 and 2920 years for E^{280}, E^{400} and E^{560}, respectively, using these old greenhouse gas levels. The time series of the Atlantic Meridional Overturning Circulation (AMOC) and global temperatures for the last 1000 years are shown on the extreme left in Fig. 2. For this study, these experiments are continued for another 1000 model years with the greenhouse gases changed to levels specified in PlioMIP2; the time series for these 1000 years are plotted on the right-hand side of Fig. 2.

3.2 Core Pliocene (Eoi^{400}) and related experiments with different CO_2 levels (Eoi^{280}, Eoi^{350} and Eoi^{450})

With greenhouse gas levels initially set to their previous values, the core experiment, Eoi^{400}, and the same experiment with pre-industrial CO_2 levels, Eoi^{280}, start from E^{280} and the model is integrated for 3000 and 1500 years, respectively. At the end of 3000 years, Eoi^{350} and Eoi^{450} branch off Eoi^{400}; the model for these two branches is integrated for 2000 years. Then as before, with greenhouse gas levels modified to PlioMIP2 values for these four experiments, the model is integrated for a further 1000 years.

The full, enhanced boundary conditions from Haywood et al. (2016) are employed; in particular, the Pliocene minus modern topography anomaly, as shown in Fig. 1, is applied to the existing MIROC4m land elevation. The largest reductions in surface elevation can be found in Greenland and parts of Antarctica, whereas the largest increases are located over North America and in the interior of Antarctica. Note that the Pliocene surface elevations used in PlioMIP1 and PlioMIP2 differ from one another (Fig. S1a in the Supplement). In addition to a lower surface elevation in the northern half of Greenland for PlioMIP2 due to a smaller ice sheet, higher surface elevation is found in southern Greenland, much of North America, except over the southern Rocky Mountains, northern Eurasia and the northern and central Andes Mountains. The land–sea mask is modified according to PlioMIP2 paleogeography. Modifications which did not exist in PlioMIP1 include the closure of the Bering Strait and the Canadian Arctic Archipelago Straits (CAAS), and the introduction of Pliocene lakes across Africa.

For consistency we apply the same vegetation distribution as that in the PlioMIP1 study by Chan et al. (2011), derived from Salzmann et al. (2008). The vegetation is extended in several regions where the land mask differs from that of PlioMIP1, for example, over an expanded Indonesia, over Beringia, resulting from a closed Bering Strait and across parts of Greenland where the ice sheets are now specified to be smaller than that of PlioMIP1. In addition, several lakes have now been included on the African continent. The bathymetry is modified by the usual anomaly method, although a separate experiment was carried out without such modifications, resulting in no noticeable differences in the climate. Soil types are changed according to their texture.

3.3 Pliocene with PlioMIP1 boundary conditions (Eplio1)

For the lone experiment with PlioMIP1 boundary conditions and CO_2 level set to 405 ppm, the model is initialised with pre-industrial conditions and integrated for 3000 years before the other greenhouse gas levels are changed to PlioMIP2 values for a further 1000 years. As in our original PlioMIP1 experiment (Chan et al., 2011), there are no modifications made to the bathymetry, soil types or lakes.

4 Results and discussion

Henceforth, we call all experiments with PlioMIP1 or PlioMIP2 boundary conditions (Eplio1 and Eoi^{xxx}) simply "Pliocene experiments", irrespective of CO_2 level. Analy-

Table 1. Boundary conditions, CO_2 levels and model integration length for each experiment in the present study.

Expt	Land–sea mask	Topography	Vegetation	Ice sheet	CO_2 (ppm)	Integration length (years)
E^{280}	Local modern	Local modern	Local pre-ind.	Local pre-ind.	280	2220
E^{400}	Local modern	Local modern	Local pre-ind.	Local pre-ind.	400	3000
E^{560}	Local modern	Local modern	Local pre-ind.	Local pre-ind.	560	3920
Eplio1	PRISM3	Local modern + PRISM3 anom.	PRISM3	PRISM3	405	4000
Eoi^{280}	PRISM4	Local modern + PRISM4 anom.	PRISM3	PRISM4	280	2500
Eoi^{350}	PRISM4	Local modern + PRISM4 anom.	PRISM3	PRISM4	350	3000
Eoi^{400}	PRISM4	Local modern + PRISM4 anom.	PRISM3	PRISM4	400	4000
Eoi^{450}	PRISM4	Local modern + PRISM4 anom.	PRISM3	PRISM4	450	3000

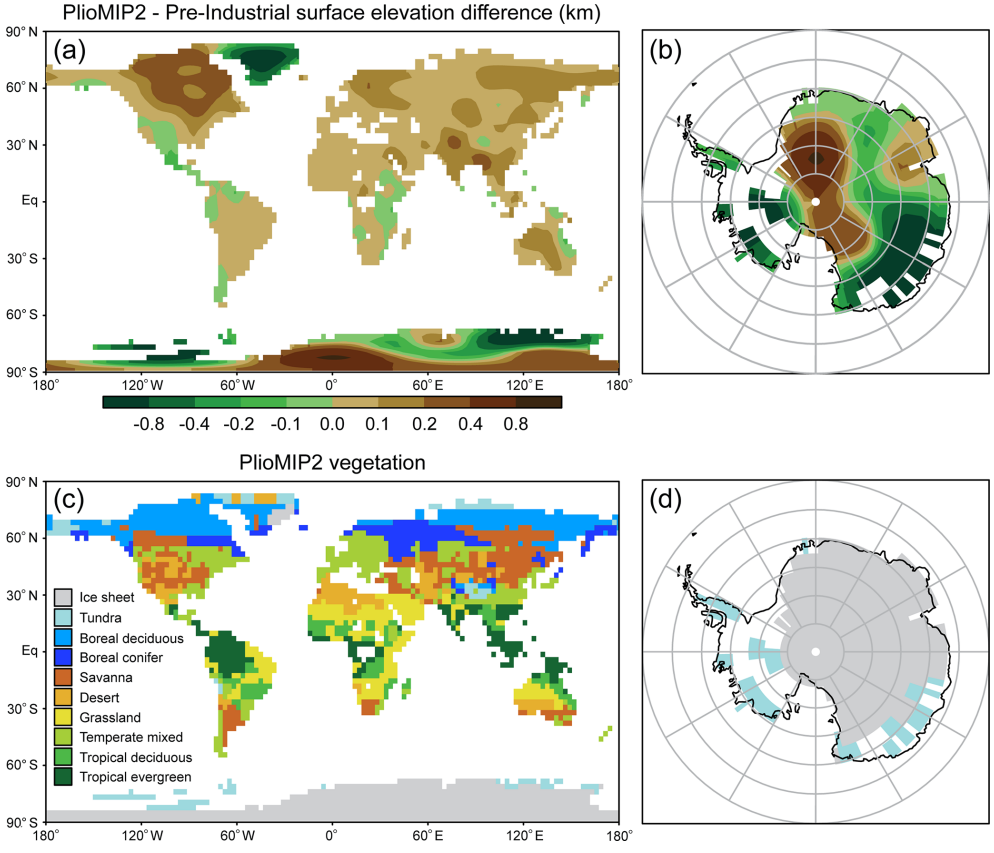

Figure 1. **(a, b)** The difference between land elevation in the Pliocene and present-day experiments and **(c, d)** the vegetation specified for Pliocene experiments on the MIROC4m grid.

ses are mostly based on the last 100 years of the model integration for each experiment and focus on the differences between the Pliocene experiments, especially the core, default Eoi^{400} experiment and the pre-industrial E^{280} experiment. We also examine the Pliocene climate for a range of CO_2 levels and determine how the Pliocene experiments, in particular the core experiment, compares with proxy data for surface air and sea surface temperatures.

4.1 Surface air temperature

The changes in the annual mean surface air temperature (SAT) from pre-industrial values are shown in Fig. 3. When only the CO_2 level is increased (Fig. 3a), temperature increases are less extreme, compared to the other experiments. E^{560}–E^{280} is not shown in this figure, but spatially, it resembles E^{400}–E^{280}. Temperature increases are slightly higher over land, with the smallest increases over central Africa and southeast Asia. Over the oceans, there are small regions,

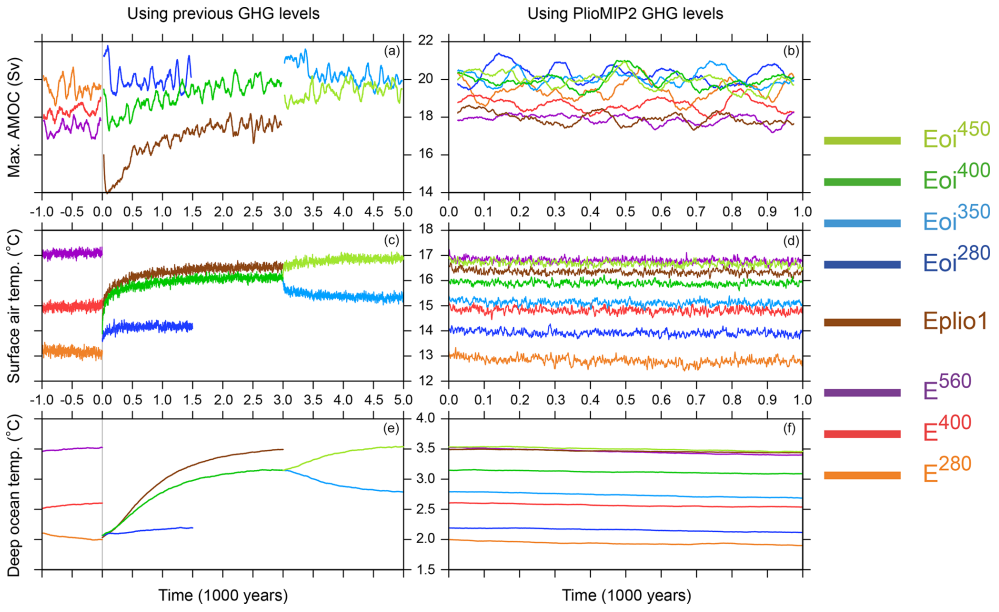

Figure 2. Time series of the AMOC index **(a, b)**, globally averaged surface air temperature **(c, d)** and global ocean temperature below depths of 1900 m **(e, f)**. A 51-year moving average has been applied to the AMOC index time series. The panels on the left depict the initial stages of the experiments during which greenhouse gas levels are set to previous, PlioMIP1 values, while the panels on the right depict the final 1000 years of the integration during which greenhouse gas levels are consistent with those specified in PlioMIP2.

Table 2. Settings common to all experiments in the present study. These refer to the last 1000 years, before which the following settings were used: 863.303 ppb CH_4, 279.266 ppb N_2O, 1366.12 W m^{-2} solar constant.

CH_4	760 ppb
N_2O	270 ppb
O_3	Local modern
Solar constant	1365 W m^{-2}
Eccentricity	0.016724
Obliquity	23.446°
Perihelion	102.04°

mainly over the Greenland Sea, where temperature changes are small, or even negative, and this is also noticeable to some extent in the other experiments. The largest temperature increases occur around the edge of Antarctica and across the Barents Sea. When only Pliocene vegetation, ice sheets, land configuration and elevation are introduced, and the CO_2 level is left unchanged, as in Eoi^{280}–E^{280} (Fig. 3c), the largest temperature increases can be found in the exact regions where ice sheets have been removed and land elevation is consequently lowered, that is, West Antarctica, the coastal regions of East Antarctica just to the south of Australia, and Greenland. Conversely, over the interior of the Antarctic continent, there are also locations where the temperature has decreased because the land elevation has increased while ice sheet is still present. Combining all Pliocene boundary conditions with increased CO_2, the spatial distribution resembles that of Eoi^{280}–E^{280}. The near-linearity of the combined effects of CO_2 and Pliocene land conditions is also reflected in the globally averaged temperature increase shown in Table 3. This increase, the global SAT anomaly, for E^{400} and Eoi^{280} is 2.0 and 1.1 °C, respectively, and that for Eoi^{400} is 3.1 °C, which corresponds to a near-zero residual from nonlinear effects, similar to the findings of Kamae et al. (2016), who further decomposed the Pliocene land conditions into ice sheets and all other effects. Others find that the combined effects are less than the sum of the individual effects (Hunter et al., 2019; Chandan and Peltier, 2018).

The overall temperature increase in Eoi^{400} is not as large as that in the PlioMIP1 experiment (Table 3), as in the case with the models HadCM3 (Bragg et al., 2012; Hunter et al., 2019), NorESM-L (Li et al., 2020) and COSMOS (Samakinwa et al., 2020), with the first model and MIROC4m both giving a PlioMIP2–PlioMIP1 global SAT difference of 0.4 °C. Other models, as noted by Li et al. (2020), show the opposite result, i.e. larger warming in PlioMIP2. In our results, overall, the PlioMIP1 temperatures lie between those of PlioMIP2 with CO_2 set to 400 and 450 ppm. PlioMIP2 temperature increases in most regions of the northern high latitudes and the tropics are smaller, and this may be at least partly a result of the increased elevation across most of the Northern Hemisphere, especially over North America, as the difference between Eoi^{400} and Eplio1 SAT follows closely that of the elevation difference (Figs. S1a and b). Conversely, SAT in Eoi^{400} is much higher than that in Eplio1 across West Antarctica, northern Green-

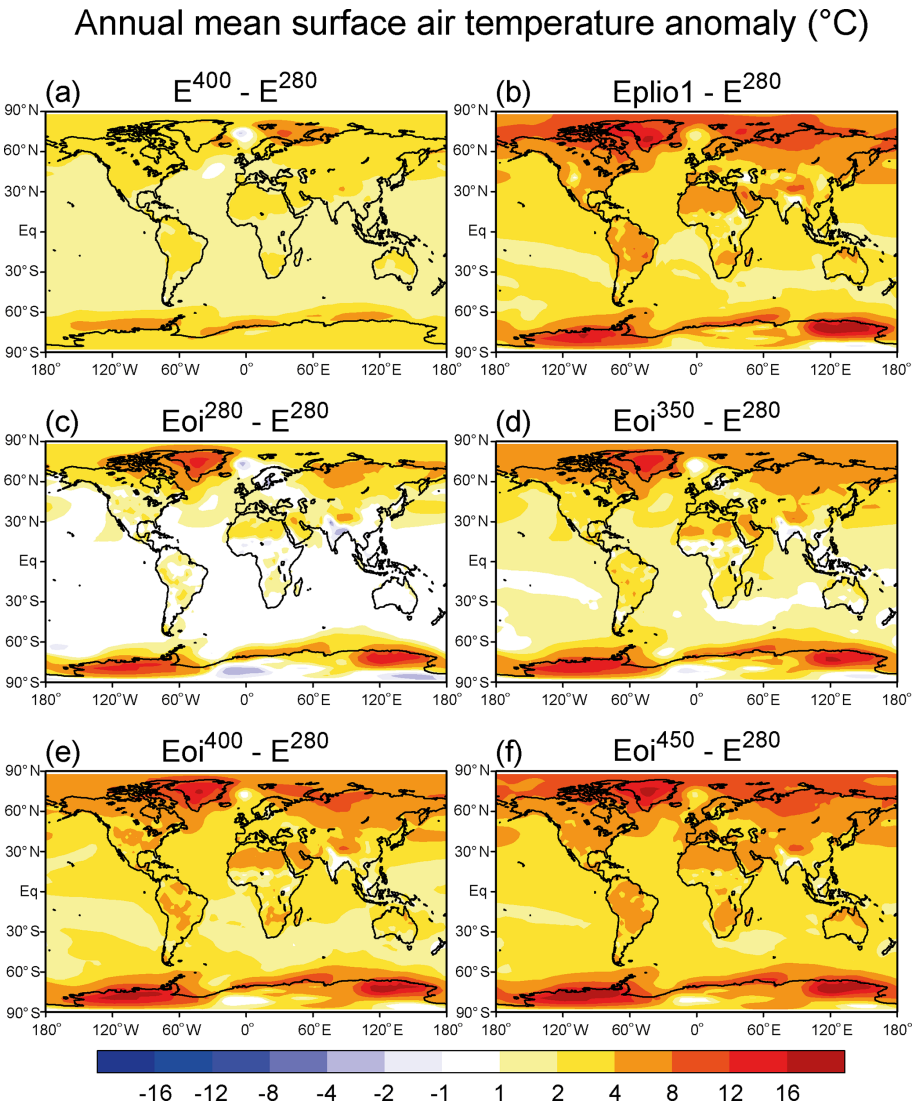

Figure 3. Annual mean surface air temperature anomaly between six experiments and E^{280}, the pre-industrial one. For a comparison of PlioMIP1 and PlioMIP2, see **(b, e)**. For the individual effects of CO_2 and Pliocene boundary conditions, see **(a, c)**, respectively.

land, the southern Rocky Mountains and the Near East, the last three of which also exhibit the same SAT differences in NorESM-L (Fig. 9a of Li et al., 2020).

The globally averaged SAT from PlioMIP has been used to estimate the Earth system sensitivity (ESS), which, unlike the climate sensitivity (CS), takes into account feedbacks operating over longer timescales (Lunt et al., 2010). From E^{280} and E^{560}, CS is estimated to be 3.9, and using Eplio1 and Eoi^{400}, ESS is estimated to be 6.6 and 6.0, respectively, and the ESS/CS ratio 1.7 and 1.5, respectively. All these values compare quite well with the PlioMIP2 multi-model mean values (Haywood et al., 2020).

Figure 4 shows the zonal mean surface air temperature increase from E^{280}. When only CO_2 is changed, a small but gradual and near-linear increase in temperature anomaly starting from the southern mid-latitudes to the northern mid-latitudes is evident (see the red and purple lines between 45° S and 45° N). The larger anomaly in the northern half is simply a consequence of the larger land area there. The increase in CO_2 is also accompanied by polar amplification of the warming. For all other experiments, the increase in temperature anomaly from the tropics to the northern mid-latitudes is more pronounced. In the northern polar region, peak warming is seen at around 75° N for all experiments. However, in the southern polar region, peak warming shifts from 65 to 75° S with the inclusion of Pliocene land elevation and reduced ice sheets. For the Pliocene experiments, Eoi^{350}, Eoi^{400} and Eoi^{450}, the increase in zonal temperature anomaly with an increase of 50ppm in CO_2 is limited to less than 1 °C at low and mid-latitudes and at most 1.5 °C in the polar regions. This increase is relatively small in comparison to results from models like IPSL-CM5A2, which shows

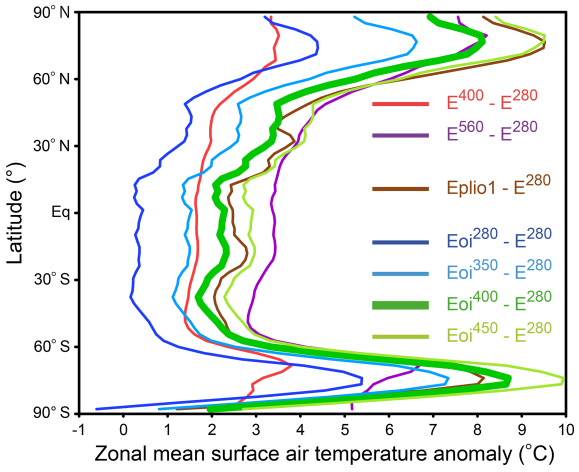

Figure 4. Zonal mean surface air temperature anomaly. The core experiment, Eoi^{400}, is shown in bold green.

a fairly small uniform change from Eoi^{350} to Eoi^{400}, except at the northern high latitudes where there is a sharp change of up to 2.5 °C (Fig. 11c of Tan et al., 2020).

The seasonal SAT anomalies for Eoi^{400} are shown in Fig. 5. There is little seasonal change over north Africa and much of the oceans. Throughout the year, temperature increases over Greenland remain large. However, there are distinct seasonal changes at high latitudes elsewhere, for example, the small temperature increase in the Arctic region during the summer, followed immediately by the extremely large temperature increase during the autumn. In the summer, there is very little sea ice in the Arctic in Eoi^{400}, and so the ocean warms up more from incoming insolation until the SST reaches a maximum. As the summer ends, heat from the ocean is released back into the atmosphere. Since there is very little sea ice, more heat can be released, explaining the higher SAT in the Arctic during September to November. This was also seen in the study by Zheng et al. (2019). The Hudson Bay shows a large temperature reduction during winter because it has been replaced by land which cannot stabilise the surface air temperature as much as water can (Hunter et al., 2019). Conversely, by the same reasoning, a large temperature increase is seen over the Hudson Bay during the summer. Another region where the temperature reduces is the zonal strip in Africa at latitude 15° N during the summer. This is similar to what was seen in the early work of Chandler et al. (1994), who attributed this feature to a weakening of the Hadley circulation. Both the summer cooling over this part of Africa and the Indian subcontinent are also clearly seen in Hunter et al. (2019).

4.2 Sea surface temperature

Annual mean sea surface temperature (SST) anomalies, shown in Fig. 6, are similar to SAT anomalies. With only an increase in CO_2 (Fig. 6a), there is a uniform increase in SST, except in the eastern Pacific and Indian Ocean sectors of the Southern Ocean, in the northwest Pacific Ocean and in the Greenland Sea. The inclusion of all other Pliocene boundary conditions leads to more extreme SST increases over the northern mid- to high latitudes, as well as the western half of the Indian Ocean. The Greenland Sea is the only region where SST decreases whether by increasing CO_2 to 400 ppm (Fig. 6a) or by introducing Pliocene boundary conditions (Fig. 6c), and this cooling persists in all the Pliocene experiments. The global SST for Eoi^{400} is 19.0 °C (Table 3), slightly lower than that for the PlioMIP1 experiment (19.2 °C).

It is later shown in Figs. S1c and S15b that SST is much lower in Eoi^{400} than in Eplio1 in the Barents Sea, along the northwest Pacific coastal regions, but much higher in the Labrador Sea, the eastern North Atlantic Ocean and parts of the Southern Ocean, which follows the SAT in the coastal regions of Antarctica. The difference in the SST of the Barents Sea in the two experiments could be explained by the higher land elevation over northern Europe in PlioMIP2 which would lead to SAT lower than those in Eplio1 in the same way higher land elevation over North America leads to SAT there being lower in Eoi^{400} than in Eplio1. The slightly warmer SST in the Labrador Sea results from the closure of the CAAS in the PlioMIP2 paleogeography since cooler waters flow southward from the Arctic Ocean to the Labrador Sea via the open CAAS in Eplio1. Not only do MIROC4m and NorESM-L show a similar warming in PlioMIP2 SST in the Labrador Sea (Fig. 9b of Li et al., 2020), but both models also show slightly higher SST in PlioMIP2 than in PlioMIP1 in coastal areas off Mexico, Chile, northwest Africa and southwest Africa, suggesting subtle differences in coastal upwelling.

4.3 Precipitation

For the Pliocene experiments, the fractional increase in the annual mean precipitation (Fig. 7) is greatest over most of Antarctica, northern Africa, the Indian Ocean, central Asia and at the northern high latitudes, in particular, across Greenland and northern Canada. Consequently, the sea surface salinity (not shown) in the Indian Ocean reduces by a large amount. Conversely, the precipitation decreases most noticeably over the oceans elsewhere, in the tropics and subtropics, in addition to the Greenland Sea where SAT decreases. Over land, the precipitation decreases across southeast North America and southern Africa. As the CO_2 level is increased, these changes are accentuated and the globally averaged precipitation increases (column 8, Table 3). The opposing changes across northern Africa and the northern South Atlantic Ocean are indicative of a northward shift of the Intertropical Convergence Zone (ITCZ). It can be seen from a comparison of E^{400}–E^{280} (Fig. 7a) and Eoi^{280}–E^{280} (Fig. 7c) that most of these changes in precipitation occur as a result of the Pliocene boundary conditions rather than the change in

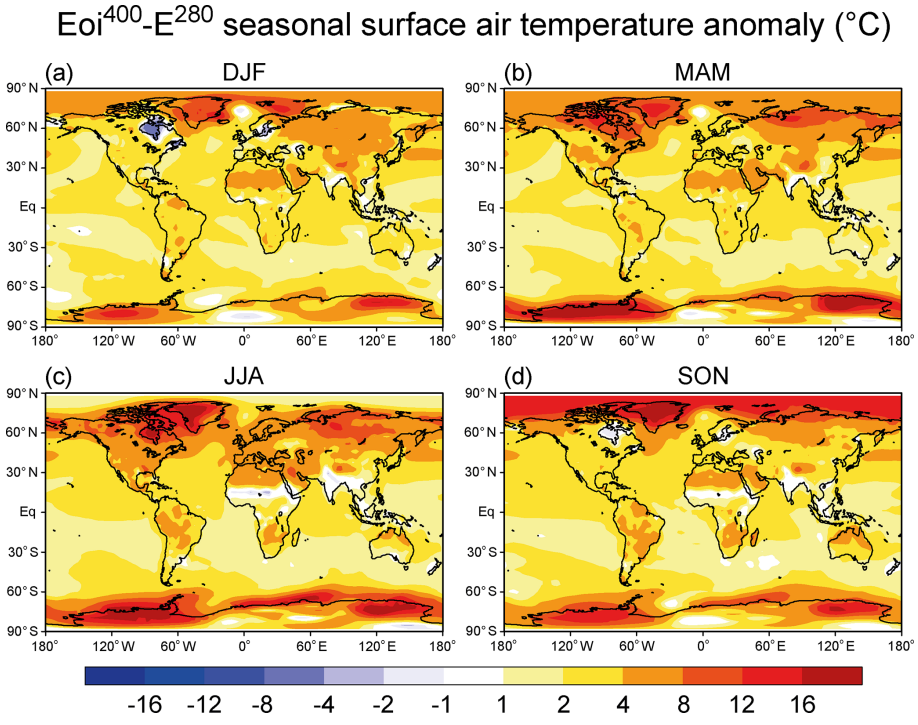

Figure 5. Seasonal surface air temperature anomaly between Eoi^{400} and E^{280} for December–February (DJF), March–May (MAM), June–August (JJA) and September–November (SON).

CO_2. The increase in CO_2 is responsible for a moderate increase in precipitation over the whole of Antarctica and for a small decrease over northern Africa, opposite to the effect of the Pliocene boundary conditions. As with SAT, the globally averaged precipitation in Eoi^{400} is larger than that in E^{280}, with CO_2 contributing about two-thirds of the total increase.

The spatial changes in the PlioMIP1 experiment are similar to those in Eoi^{400}, with the global changes in precipitation also being similar (Table 3). However, there are small differences in the amount of precipitation change (Fig. S1d). In many areas, precipitation increases with decreasing surface elevation and vice versa, for example, over Greenland and Antarctica. Eoi^{400} precipitation is lower in the Indian Ocean, west of Australia, while it is higher in northern Africa and the tropical Atlantic. This may be related to differences in the ITCZ.

4.4 Sea ice and ocean mixed layer depth

The total sea ice area in the polar regions is depicted in Fig. 8. In the Arctic, during March when the sea ice area is at its greatest, there is a gradual decrease in area as CO_2 is increased, whether pre-industrial or Pliocene boundary conditions are used. The sea ice area in Eplio1 is actually larger than any of the other Pliocene experiments because the land area around the Arctic is smaller in Eplio1, as can be seen later in Fig. 9 – the Bering Strait is open, the Hudson Bay is still set as open water, and the Labrador Sea is larger and connected to the Arctic Ocean. During September, when the sea ice area is at its smallest, a similar trend is observed. The Arctic Ocean is ice-free in Eplio1, Eoi^{400} and Eoi^{450}. In the Antarctic, during September, the decrease in sea ice area as CO_2 increases is much more drastic. The Antarctic sea ice area when the CO_2 level is doubled is also much lower than that of any of the Pliocene experiments. Unlike the Arctic, the sea ice area in Eplio1 and Eoi^{400} are similar as the Antarctic coastlines in the two cases do not differ by much. The same behaviour is observed in March, although unlike in the Arctic, the Antarctic is never ice-free. However, in both polar regions, the boundary of sea ice extent in Eoi^{400} and Eplio1 is similar (Figs. 9 and 10).

The sea ice extent in the Arctic and the mixed layer depth (MLD) in the surrounding regions during March are shown in Fig. 9. The definition of the MLD follows that of Oka et al. (2006), i.e. the depth at which σ_θ, the potential density anomaly, differs from the surface value by 0.1. The sea ice extent here is largely unaffected by the Pliocene boundary conditions alone and only recedes near the northwest Pacific coastline and in the Barents Sea as CO_2 is increased. In E^{280}, the MLD is large everywhere south of the sea ice extent in the North Atlantic, including the Labrador Sea and the Norwegian Sea, and to a lesser extent west of the British Isles. The Labrador Sea responds with a larger MLD, spread over a greater area directly south of Greenland, to Pliocene boundary conditions and increasing CO_2. when applied separately. However, when both Pliocene boundary conditions

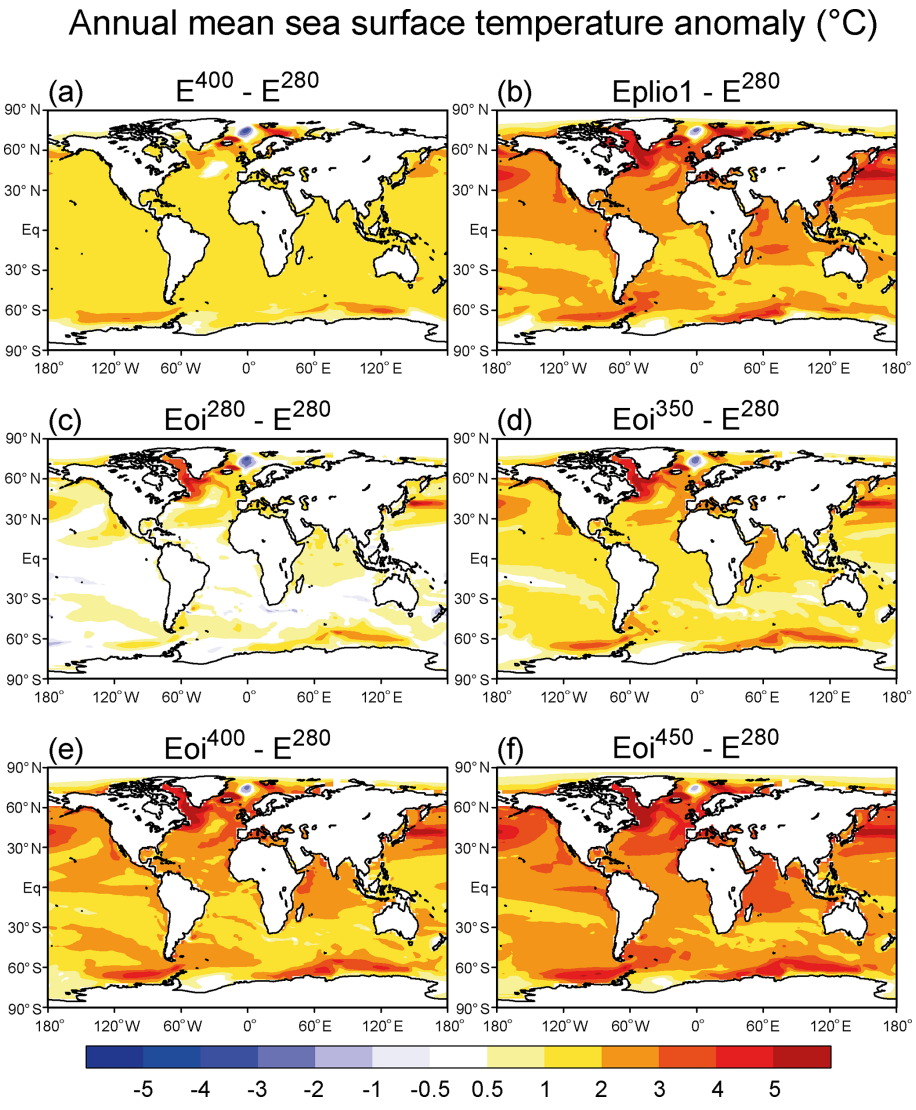

Figure 6. Annual mean sea surface temperature anomaly between six experiments and E^{280}, the pre-industrial period. For a comparison of PlioMIP1 and PlioMIP2, see **(b, e)**. For the individual effects of CO_2 and Pliocene boundary conditions, see **(a, c)**, respectively.

and changes in CO_2 are applied, as in Fig. 9e–h, it can be seen that CO_2 has an opposing effect on the MLD, suggesting that deepwater formation in the Labrador Sea is greater in Eoi^{280} than in Eoi^{450}. In the Eplio1 experiment, lower SST in the Labrador Sea, as discussed previously, also contributes to greater deepwater formation so that the MLD is more comparable to that of Eoi^{280}. In the Norwegian Sea, the areal extent of deep MLD is similar in all experiments, but only E^{280} shows the maximum MLD of about 3000 m, located at the northernmost ice-free region, at latitude 80° N. In all experiments with higher CO_2, the sea ice in the northeast of the Norwegian Sea retreats and exposes the Barents Sea, but the extent of the deepwater formation region in the Norwegian Sea remains unchanged. In the region to the west of the British Isles, regardless of CO_2 level, no change is seen when PlioMIP2 boundary conditions are applied. On the other hand, there is little deepwater formation there in Eplio1 or when the CO_2 level is 400 ppm or higher with present-day boundary conditions.

The sea ice extent and MLD in the Antarctic during September are shown in Fig. 10. With present-day boundary conditions (E^{280}, E^{400} and E^{560}), the MLD is extremely large in the Atlantic sector of the Southern Ocean, even below parts of the sea ice in E^{280}, suggesting the formation of dense water due to brine rejection. In the Pliocene experiments, this large MLD is absent, while in the other region where the MLD is large with present-day boundary conditions, i.e. the eastern South Pacific, it is reduced.

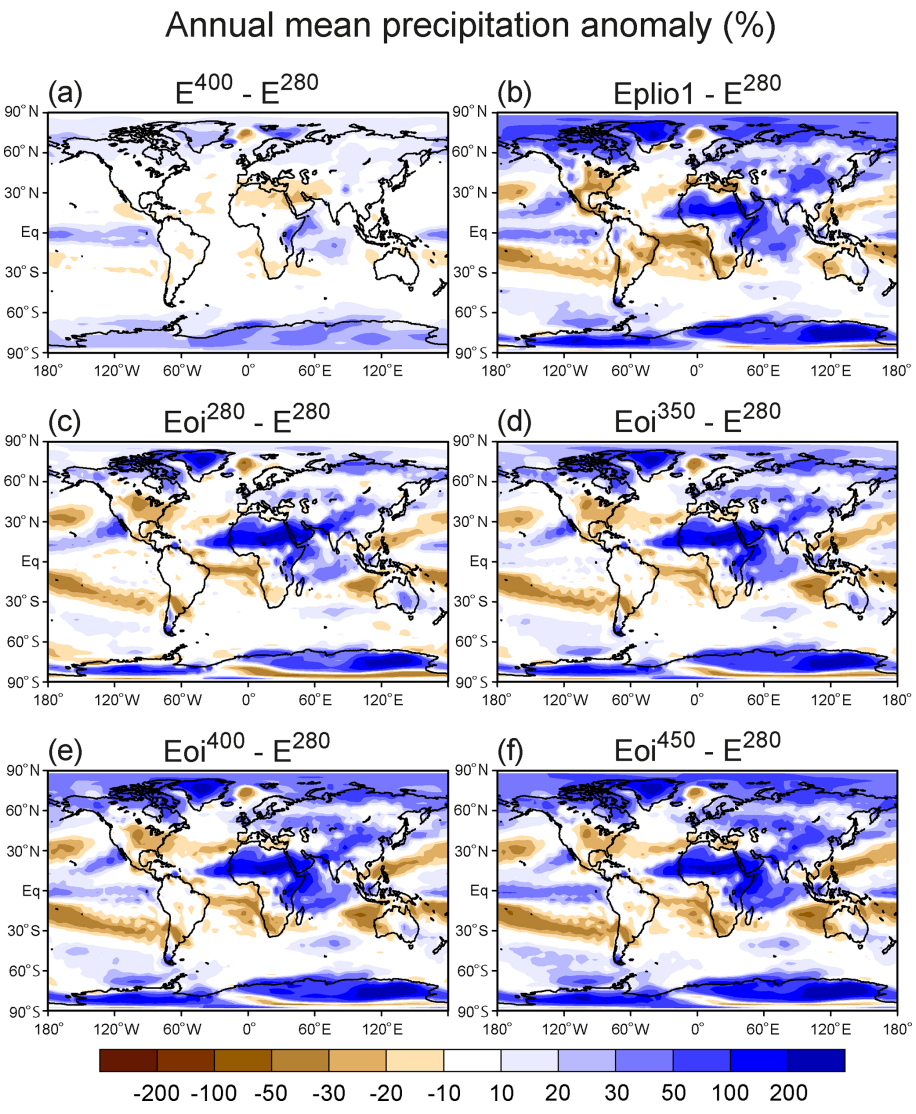

Figure 7. Annual mean precipitation anomaly between six experiments and E^{280}, the pre-industrial one, as a percentage of E^{280}, e.g. $100 \times (Eoi^{400} - E^{280})/E^{280}$. For a comparison of PlioMIP1 and PlioMIP2, see **(b, e)**. For the individual effects of CO_2 and Pliocene boundary conditions, see **(a, c)**, respectively.

4.5 Atlantic meridional overturning circulation

The AMOC is shown in Fig. 11, and the AMOC index, defined as the maximum streamfunction value, is shown in the last column of Table 3. Increasing the CO_2 level alone has a tendency to weaken the AMOC. As the overturning cell becomes shallower, the underlying Antarctic Bottom Water extends further northward. In addition, the anti-clockwise overturning cell north of 65° N strengthens, contributing to increased convection and deepwater formation in the Labrador Sea, as indicated by the MLD in Fig. 9. A comparison of Eoi^{280} with E^{280} shows that similar changes occur when only the Pliocene boundary conditions are applied, except that the AMOC index increases by nearly 0.7 Sv, despite shoaling of the AMOC. Thus, increasing CO_2 and applying Pliocene boundary conditions have an opposite effect on the AMOC index, but up to 450 ppm CO_2, the indices for all the Pliocene experiments are still greater than that for E^{280}. Note that the degree of weakening in the AMOC as CO_2 increases seems to be highly dependent on the boundary conditions. With present-day boundary conditions, from E^{280} to E^{400}, the AMOC index decreases by 0.8 Sv, whereas in the corresponding Pliocene experiments, Eoi^{280} and Eoi^{400}, there is only a decrease of approximately 0.2 Sv (Table 3).

A comparison of Eoi^{400} and Eplio1 shows that while the AMOC cell extends to similar depths and the circulation in the other two cells changes little, the AMOC index with PlioMIP2 boundary conditions is larger than that with PlioMIP1: 20.0 Sv versus 17.8 Sv. While we have not performed specific sensitivity experiments to see what differ-

Table 3. Global mean and other values for each experiment, averaged over the last 100 years. From left to right, the columns show the following: (1) experiment name, (2) global surface air temperature, (3) global surface air temperature anomaly with E^{280} as the reference, (4) surface air temperature averaged over latitudes 60–90° N, (5) surface air temperature averaged over latitudes 30° S–30° N, (6) surface air temperature averaged over latitudes 90–60° S, (7) energy balance at the top of the atmosphere, (8) global precipitation, (9) global sea surface temperature, (10) global ocean temperature averaged across all depths, and (11) AMOC index. The AMOC index is averaged over the last 500 years to remove large centennial variability, as seen in Fig. 2.

Expt	Global SAT (°C)	Global ΔSAT (°C)	North SAT (°C)	Tropical SAT (°C)	South SAT (°C)	TOA en. bal. ($W m^{-2}$)	Global precip. ($mm d^{-1}$)	Global SST (°C)	Global ocean T (°C)	AMOC index (Sv)
E^{280}	12.8	0.0	−11.4	23.0	−18.4	0.88	2.69	17.0	1.91	19.5
E^{400}	14.8	2.0	−8.1	24.7	−15.3	0.96	2.79	18.4	2.54	18.7
E^{560}	16.8	3.9	−4.2	26.5	−12.7	1.02	2.90	19.9	3.40	17.8
Eplio1	16.3	3.5	−3.0	25.7	−12.3	0.85	2.87	19.2	3.44	17.8
Eoi^{280}	13.9	1.1	−7.7	23.5	−15.0	0.80	2.74	17.5	2.12	20.2
Eoi^{350}	15.1	2.3	−5.7	24.6	−12.2	0.83	2.81	18.4	2.69	20.0
Eoi^{400}	15.9	3.1	−4.4	25.4	−12.0	0.84	2.86	19.0	3.09	20.0
Eoi^{450}	16.6	3.8	−3.2	26.0	−11.0	0.84	2.90	19.6	3.46	19.8

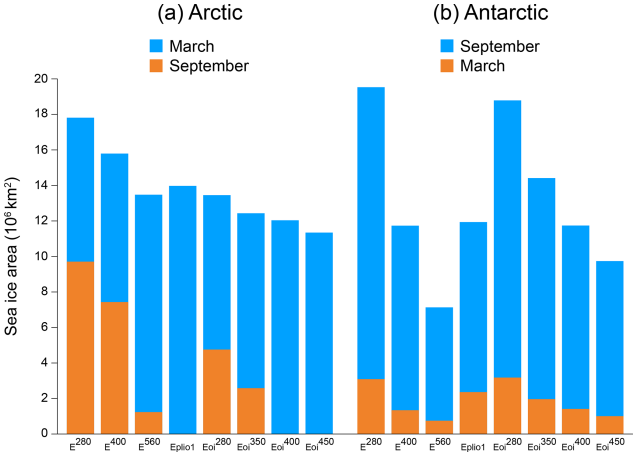

Figure 8. Total surface area of sea ice in each polar region during March and September.

ence between the PlioMIP1 and PlioMIP2 boundary conditions is exactly responsible for this difference in the AMOC index, we did perform some (not shown) with a pre-industrial background climate and looked at the effects of closing the Bering Strait and the CAAS. We find that, as in Pliocene studies by Otto-Bliesner et al. (2017), the closure of the Bering Strait, irrespective of the state of the CAAS, leads to a stronger AMOC. Closing the Bering Strait inhibits the transport of freshwater from the North Pacific Ocean via the Arctic Ocean and increases the AMOC index by 1–2 Sv in the MIROC4m experiments, and so it likely explains the difference between Eoi^{400} and Eplio1. This increase is sufficient to give a stronger Pliocene AMOC when compared to the pre-industrial period, a result which is opposite to when using PlioMIP1 boundary conditions and which is consistent with recent PlioMIP2 simulations with other models (e.g. Chandan and Peltier, 2017; Tan et al., 2020; Hunter et al., 2019; Li et al., 2020; Feng et al., 2020).

4.6 Meridional heat transport

Figure 12a shows the meridional ocean heat transport in the Atlantic Ocean for E^{280} and the Pliocene experiments. The transport peaks at around 0.7 PW, near latitude 15° N. Figure 12b shows the difference between the same heat transport in the Pliocene experiments and E^{280}. In all the Pliocene experiments, there is a reduction in the heat transport at all latitudes, with the greatest reduction at the Equator for experiments using PlioMIP2 boundary conditions. For these four PlioMIP2 Pliocene experiments, there does not appear to be any general trend as the CO_2 level is increased. For example, Eoi^{450} has a significantly lower heat transport compared to the others south of the Equator, whereas at the northern low to mid-latitudes, Eoi^{450} values are rather close to those of Eoi^{400} and it is the Eoi^{280} values that stray from the rest. It can also be seen that there is a marked difference between the heat transport in Eplio1 and those using PlioMIP2 boundary conditions. At all latitudes south of 30° N, heat transport in Eplio1 is about 0.1 PW lower than that of E^{280}. Irrespective of CO_2 level, this larger difference can mostly be attributed to the differences between the PlioMIP1 and PlioMIP2 boundary conditions, as can the difference between the AMOC index of Eplio1 and those of the PlioMIP2 Pliocene experiments. However, as noted in the latter experiments, the northward heat transport decreases even though the AMOC index increases, albeit to a relatively small degree. While these two properties are commonly thought of as being positively correlated to each other, Sévellec and Fedorov (2016) show that this is not always the case. Using NorESM-L, Eoi^{400} exhibits the same features, i.e. reduced meridional heat transport in the Atlantic Ocean but a stronger AMOC (Li et al., 2020),

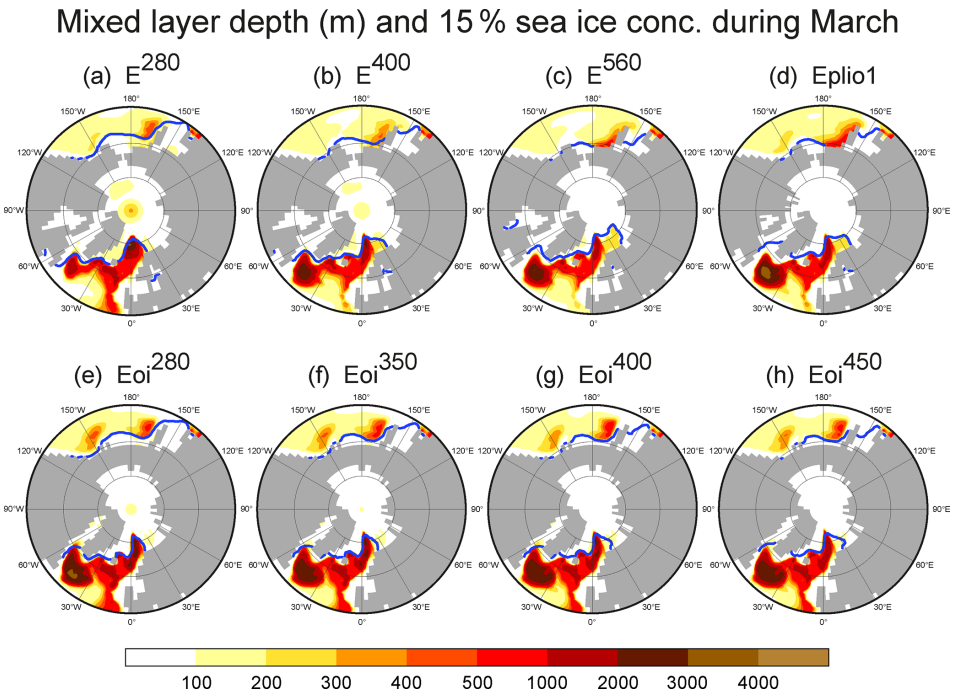

Figure 9. Oceanic mixed layer depth in the Northern Hemisphere during March. The blue lines indicate the extent of 15 % sea ice concentration. For a comparison of PlioMIP1 and PlioMIP2, see **(d, g)**. For the individual effects of CO_2 and Pliocene boundary conditions, see **(b, e)**, respectively.

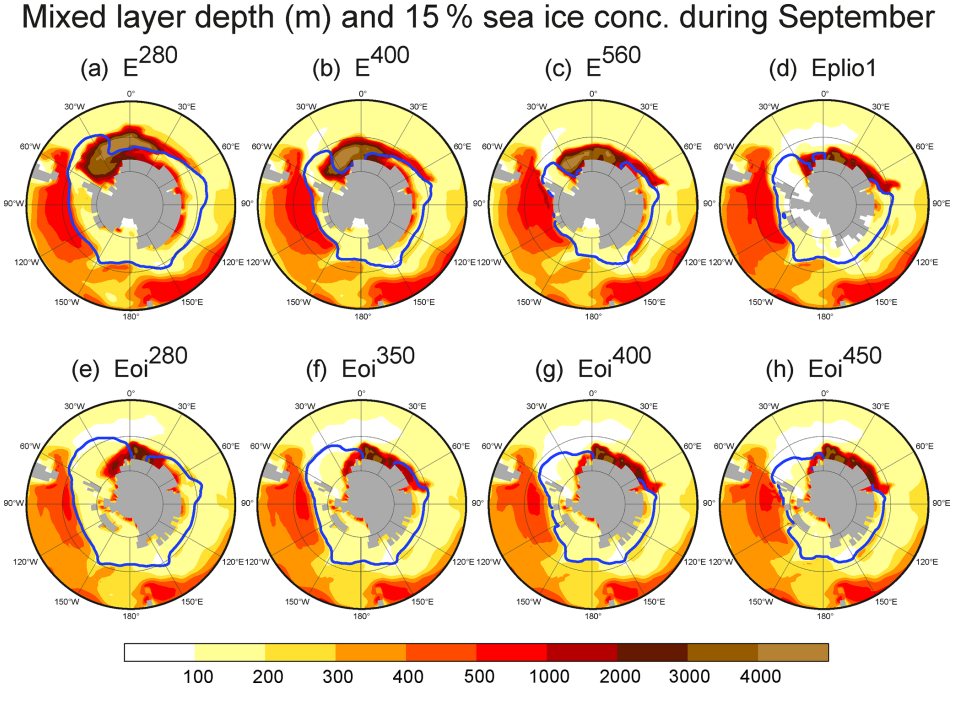

Figure 10. Oceanic mixed layer depth in the Southern Hemisphere during September. The blue lines indicate the extent of 15 % sea ice concentration. For a comparison of PlioMIP1 and PlioMIP2, see **(d, g)**. For the individual effects of CO_2 and Pliocene boundary conditions, see **(b, e)**, respectively.

whereas its sister model, NorESM1-F, as well as many other models, show both increased heat transport and a stronger AMOC (Kamae et al., 2016; Chandan and Peltier, 2017; Tan et al., 2020).

Figure 13 shows the total meridional heat transport in a similar way but for the whole climate system, combining atmosphere and ocean. The absolute values, in Fig. 13a, confirm that, in general, heat is transported northwards in the Northern Hemisphere and southwards in the Southern Hemisphere. In some studies, the total heat transport in both hemispheres in Eoi^{400} either decreases (Chandan and Peltier, 2017) or increases (Feng et al., 2020). In contrast, for all Pliocene experiments in this study, northward heat transport is reduced in the Northern Hemisphere, while southward heat transport is increased in the Southern Hemisphere (Fig. 13b). This appears to be more akin to the results from IPSL-CM5A, as seen in Fig. 6a of Tan et al. (2020), although the anomalies are not shown in their study explicitly. How these individual experiments differ from one another depends on the hemisphere. Firstly, with PlioMIP2 boundary conditions, as the CO_2 level is increased, there is a clear, monotonous trend with the magnitude of the northward heat transport anomaly reducing in the Northern Hemisphere. The opposite trend is seen in the Southern Hemisphere as southward heat transport increases with CO_2. Eoi^{400} represents a half-way mark whereby the bold green line in Fig. 13b is roughly symmetric across the Equator. Secondly, Eplio1 aligns very closely with Eoi^{400} in the Southern Hemisphere, whereas in the Northern Hemisphere, Eplio1 sets itself apart from the other Pliocene experiments and its heat transport reduces much less. Finally, we note that the largest anomalies occur at low latitudes, a characteristic not evident in the studies mentioned above which tend to show greatest anomalies at the mid-latitudes where the absolute values are at their peak.

4.7 Comparison with surface air temperature proxy data

In Fig. 14, the annual mean SAT from the Pliocene experiments and E^{280} are compared with SAT estimates from vegetation reconstructions at marine sites near land, as compiled by Salzmann et al. (2013). The red symbols refer to the PlioMIP2 Pliocene experiments, with the lower and higher horizontal red lines referring to 350 and 450 ppm CO_2, respectively. For most locations, SATs from these experiments show the correct tendency and agree better with the proxy data than E^{280}. Locations where the Pliocene values do not match proxy data as well as E^{280} values include Rio Maior, Yorktown and Pinecrest, where the Pliocene values are too high and proxy data values are very close to E^{280} values. However, the biggest discrepancies are seen in the Charan Basin and Lake Baikal, but even here, the Pliocene values match proxy data better than E^{280} values. Moreover, the Pliocene model values at these two locations are very close to the CCSM4 model results in Table 4 of Chandan and Peltier

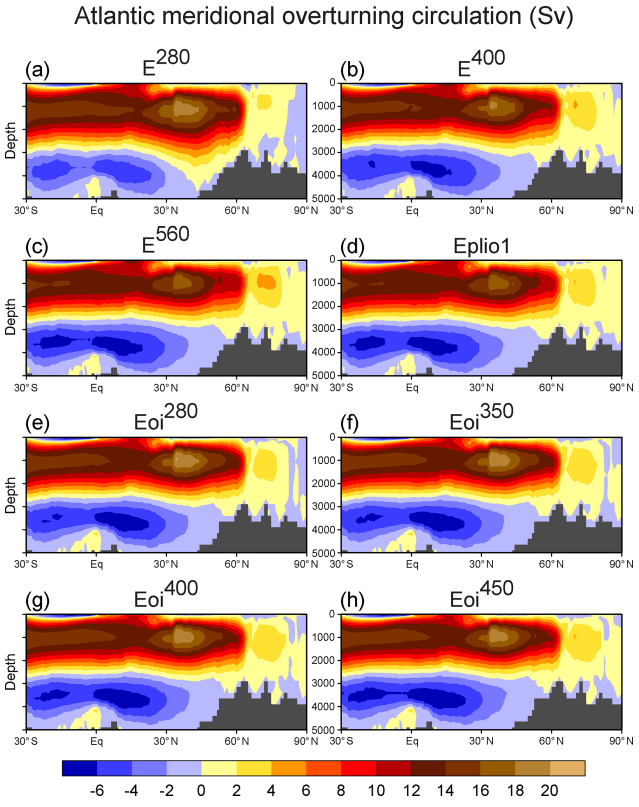

Figure 11. Streamfunction of the Atlantic meridional overturning circulation, averaged over the last 500 years. For a comparison of PlioMIP1 and PlioMIP2, see **(d, g)**. For the individual effects of CO_2 and Pliocene boundary conditions, see **(b, e)**, respectively.

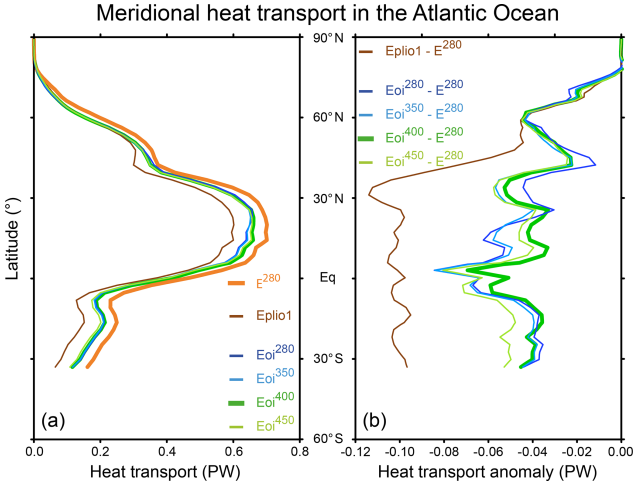

Figure 12. **(a)** The Atlantic Ocean meridional heat transport in the Pliocene experiments and in E^{280} and **(b)** the anomaly between the Pliocene experiments and E^{280}. The core experiment, Eoi^{400}, is shown in bold green.

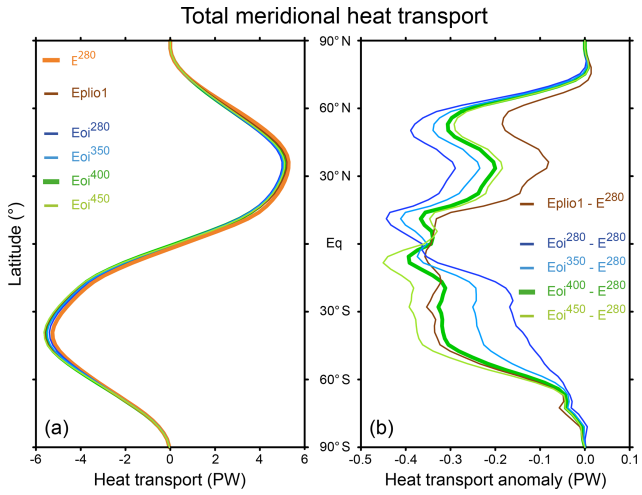

Figure 13. **(a)** The total meridional heat transport in the Pliocene experiments and in E^{280}, as calculated from the top-of-atmosphere radiative transport, and **(b)** the anomaly between the Pliocene experiments and E^{280}. The core experiment, Eoi^{400}, is shown in bold green.

Table 4. The difference between the annual mean SST anomaly (from E^{280}) of each experiment and the equivalent from the PRISM3 proxy data. Positive values signify that the increase in model SST is greater than the increase in proxy SST. Units are degrees Celsius. The PRISM3 proxy data were used as SST boundary conditions for AGCM experiments in PlioMIP1.

Experiment	Global	90–60° N	30° N–30° S	60–90° S
Eplio1	1.05	−1.28	2.19	0.04
Eoi^{280}	−0.76	−3.03	0.23	−1.08
Eoi^{350}	0.14	−4.43	1.21	−0.35
Eoi^{400}	0.76	−1.92	1.88	0.20
Eoi^{450}	1.31	−1.40	2.43	0.74

(2017). There are many locations where the Pliocene SATs, in particular that of Eoi^{400}, fall within the proxy data uncertainty range, which, in turn, is significantly higher than the E^{280} values, e.g. Andalucia G1, Habibas and Nador. Eplio1 values, for the most part, are similar to Eoi^{400} or Eoi^{450} values. Thus, in general, the Pliocene experiments show good agreement with the proxy data, but there does not appear to be any particular value of CO_2 which gives the best fit.

A similar comparison between model SAT and estimates from terrestrial vegetation data in the same study is shown in Fig. 15. The sites in the figure are listed according to latitude, following Table S3a of Salzmann et al. (2013), with those on the left being located at northern high latitudes. At the most northerly sites (1–10, as numbered at the top of Fig. 15), most of which are located in Alaska and Siberia, model SAT increases by at least 5 °C, consistent with the warming suggested by the vegetation data, but the degree of warming is insufficient. As noted before, Eplio1 SAT is higher than SAT from the other Pliocene experiments at northern high latitudes. At sites 11–20, located at latitudes 56—47° N, the degree of warming is, in most cases, sufficiently high such that Pliocene SATs at higher levels of CO_2 fall within the range of SAT derived from vegetation data. At the remaining sites, further south, Pliocene warming is also seen, although there are some sites (e.g. 26–28) where pre-industrial SAT is already equal to or higher than the proxy value.

4.8 Comparison with sea surface temperature proxy data

PRISM SST proxy data from a variety of marine sources have formed an integral part of PlioMIP, as boundary conditions for AGCM experiments in the first phase and, more importantly, as part of data–model comparison. Figure 16a compares the annual mean Eoi^{450}–E^{280} SST anomalies with the corresponding anomalies from PRISM3 sites where the colour refers to the difference between these two anomalies, with yellow, orange and red meaning model SST anomalies are greater. The symbols show whether the proxy anomalies suggest a warmer Pliocene (triangles) or a cooler Pliocene (circles). Only a few PRISM3 sites show a cooler Pliocene, at low latitudes, and Eoi^{400} does not replicate this cooling, especially in the Indian Ocean. In general, there is good agreement in the Southern Ocean where proxy data suggest a warmer Pliocene. In the Northern Hemisphere, where PRISM3 sites also suggest a warmer Pliocene, Eoi^{400} overestimates the SST increase by up to 3 °C in parts of the southern North Atlantic. As with model results from PlioMIP1, the large degree of warming in the northern North Atlantic and Greenland Sea is not replicated (blue triangles). A comparison of Eoi^{400} and Eplio1 SST anomalies is shown by the colours in Fig. 16b. SST anomalies in Eoi^{400} are larger mainly in the Indian and Pacific sectors of the Southern Ocean, the eastern Atlantic Ocean, and the Labrador Sea. While the SST anomalies in much of the northern North Atlantic and the Barents Sea are lower in Eoi^{400} compared to Eplio1, the Eoi^{400} values at the PRISM3 sites are actually higher and thus agree better with the proxy data, as shown by the yellow triangles.

We also include a similar comparison between model results and the newer PRISM4 proxy SST data sets (Foley and Dowsett, 2019) in Fig. 17. The degree of warming in Eoi^{400} is much less than that suggested by PRISM4 proxy data in the Atlantic sites, in particular, at northern high latitudes again, and also near southern Africa. Slightly higher warming in Eoi^{400} is generally seen at the other sites, mostly located at low latitudes, but especially in the Caribbean Sea, which is not so evident in the PRISM3 comparison (Fig. 16a). The PRISM4 data used here refer to the broader 30 kyr interval, but alternative data for a 10 kyr interval give the same conclusions. Qualitatively speaking, at least, these results are similar to those obtained from the multi-model mean in Fig. 8c of Haywood et al. (2020).

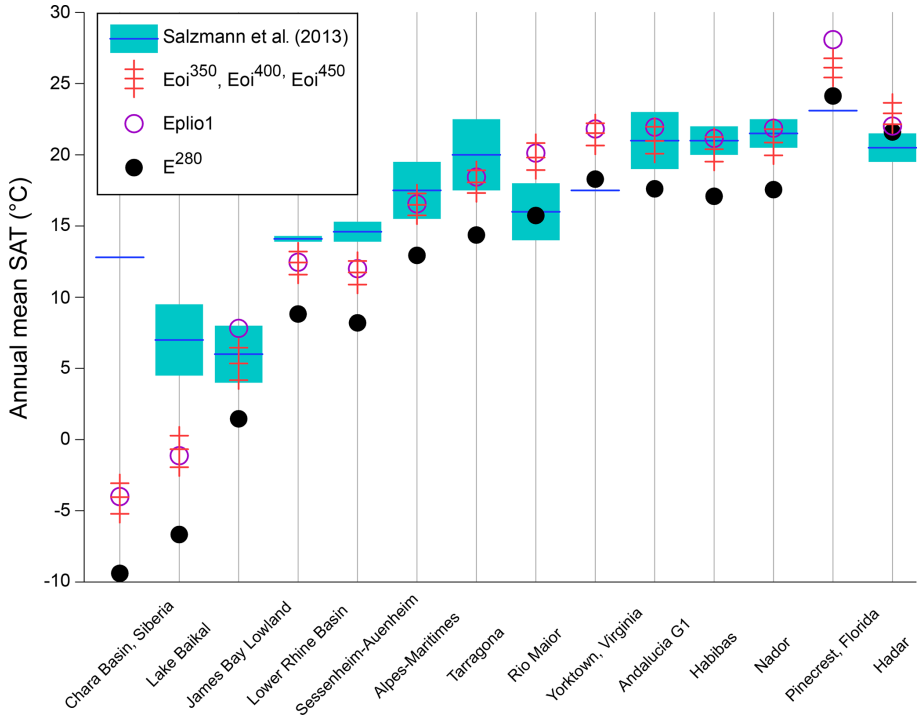

Figure 14. Comparison of annual mean surface air temperatures derived from marine proxy data (Table S3b of Salzmann et al., 2013) and those from model experiments. Proxy data are indicated by the dark blue line and the uncertainty range by light blue. The three red marks represent, from top to bottom, E^{450}, E^{400} and E^{350}.

For a more global sense of how the various Pliocene experiments compare with the proxy data, we refer back to the global PRISM3 SST field which was used as boundary conditions for AGCM experiments in PlioMIP1 and list the spatially and annually averaged model–data difference in Table 4. An important caveat here is that this global SST field is reconstructed from data at a finite number of sites for February and August using interpolation and extrapolation and that there are regions where data are sparse (Dowsett et al., 1999). Comparing Eplio1 and Eoi^{400}, we see that the former matches the proxy data better at northern high latitudes and even better at southern high latitudes (a difference of only 0.04 °C). On the other hand, the latter shows a smaller discrepancy in the tropics and low latitudes (30° S–30° N), where the larger surface area means that, globally speaking, Eoi^{400} gives a better fit (a difference of 0.76 °C). Next, a comparison of Eoi^{350}, Eoi^{400} and Eoi^{450} shows that, while there is a trend in the model–data difference as CO_2 is reduced, there is no particular level at which the difference is small at the three latitudinal ranges in Table 4. Since the global difference is determined more by the low latitudes, Eoi^{350} gives the best global fit (a difference of 0.14 °C). It is worth noting that, not only does Eoi^{280} give the best fit at low latitudes, but the discrepancy is smaller than that for Eoi^{350} at northern high latitudes, despite the increasing trend in discrepancy from Eoi^{450} to Eoi^{350}.

For reference, the discrepancies between the model and proxy SST anomalies at the PRISM3 sites for different CO_2 levels are shown in Fig. S2. Similarly, comparisons using PRISM4 data for different CO_2 levels are shown in Fig. S3. There is no spatial reconstruction to accompany the data from PRISM4 sites, and so comparisons are based solely on these sites. Lower values of CO_2 tend to give better agreement at low latitudes, except to the west of western Africa where Eoi^{450} shows good agreement. However, even in Eoi^{450}, Pliocene warming in the Greenland and Norwegian Seas, the northern North Atlantic Ocean, and the coastal region near southern Africa is much lower than that suggested by PRISM4 data (blue triangles).

More recent studies by Tierney et al. (2019) have highlighted uncertainties in tropical SST estimates and showed good agreement between their reduced space reconstruction and a Pliocene simulation run with CESM1. We carry out an SST comparison (Fig. 18) between our Pliocene experimental results and their reconstruction, limited to the Pacific Ocean, using alkenone proxy data and a probabilistic approach. In the tropical Pacific, this proxy reconstruction exhibits higher temperature anomalies than those from PRISM3, leading to optimal agreement with Eoi^{400} (Fig. 18c), which was warmer than PRISM3 data by 1–3 °C in that same region (not shown). Although the proxy reconstruction shows enhanced warming in the eastern equatorial Pacific and in the northern subtropical Pacific, this warming

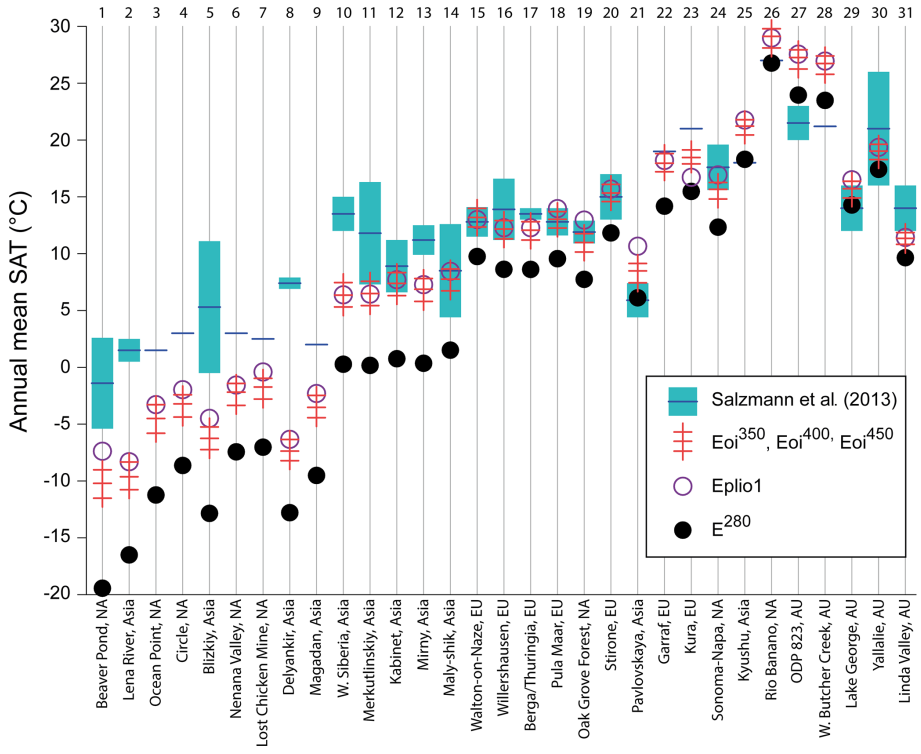

Figure 15. Comparison of annual mean surface air temperatures derived from terrestrial proxy data (Table S3a of Salzmann et al., 2013) and those from model experiments. Proxy data are indicated by the dark blue line and the uncertainty range by light blue. The three red marks represent, from top to bottom, E^{450}, E^{400} and E^{350}. Abbreviations used at the bottom of the figure: NA: North America; EU: Europe; AU: Australia.

is underestimated by 1–3 °C, compared to PRISM3. This is most evident in the northwest Pacific where the reconstruction has more limited data, and warming is weaker than that in all our Pliocene experiments.

5 Summary and conclusions

In the present study, we have shown some basic results from the core PlioMIP2 experiment using the MIROC4m AOGCM, comparing them to results from both the PlioMIP1 experiment and some other Tier 1 and Tier 2 PlioMIP2 sensitivity experiments. Additionally, we have evaluated the consistency between these experimental results and some temperature proxy data from marine and terrestrial sources.

For the core experiment, PlioMIP2 boundary conditions produce a global temperature increase smaller than that with PlioMIP1, and it can be assumed that the CO_2 level has little effect as it differs only slightly in the two phases of PlioMIP. The difference in the results from these two experiments is not uniform as greater warming is seen in PlioMIP2 in parts of the northern high latitudes and of the Southern Ocean. Moreover, PlioMIP2 SSTs can actually be reconciled better with proxy-derived values at PRISM3 sites in the northern North Atlantic and Greenland Sea, albeit to a very small degree, although the large discord in the northern North Atlantic Ocean SSTs still remains. For SAT, both PlioMIP1 and PlioMIP2 values show fairly good agreement with proxy data from paleobotanical sites, although comparisons at the northern high-latitude sites highlight the weaker polar amplification in model results. Northern polar amplification is slightly less in PlioMIP2, but nonetheless, zonal SAT increases are more than double that of the low latitudes. Our sensitivity experiments have only distinguished between the two forcings from CO_2 and Pliocene boundary conditions, and we have not considered the effects from the ice sheets, orography and vegetation separately. CO_2 accounts for two-thirds of the total surface air temperature and precipitation increase. Unlike PlioMIP1, the AMOC in PlioMIP2 is stronger compared to the pre-industrial period for MIROC4m, which is in line with other model results published so far in PlioMIP2. The strengthening of the AMOC from PlioMIP1 to PlioMIP2 is tied to the closure of the Bering Strait.

We have also looked at the mid-Pliocene climate for a range of CO_2 values. From these CO_2 sensitivity experiments, we find that, not only does the AMOC strength decrease with increasing CO_2, but this dependency on CO_2 is weaker when Pliocene boundary conditions are applied. While other expected trends are seen, such as the increase in global temperature and precipitation with CO_2, the comparison with proxy-derived data is of great importance. Mis-

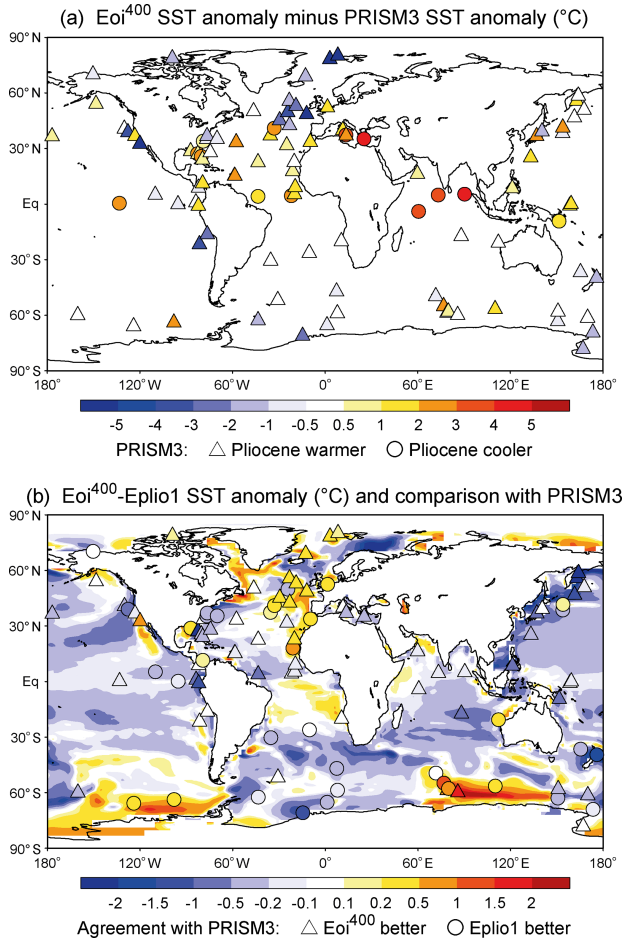

Figure 16. **(a)** Comparison of annual mean model SST anomalies and PRISM3 proxy data SST anomalies. Blue (red) indicates that model SST anomalies are smaller (greater) than those of proxy data. The shape of the symbols indicates whether proxy data suggest higher (triangle) SST in the Pliocene or lower (circle). **(b)** The difference between PlioMIP1 and PlioMIP2 SST. The shape of the symbols at PRISM3 locations indicates whether PlioMIP2 agrees better with proxy data (triangle) or whether PlioMIP1 agrees better (circle).

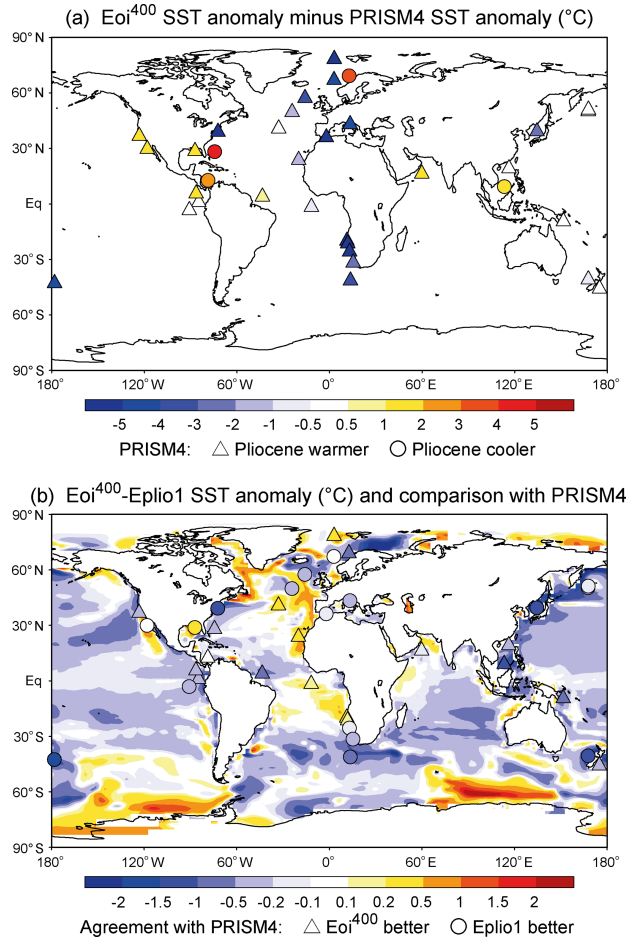

Figure 17. **(a)** Comparison of annual mean model SST anomalies and PRISM4 proxy data SST anomalies. Blue (red) indicates that model SST anomalies are smaller (greater) than those of proxy data. The shape of the symbols indicates whether proxy data suggest higher (triangle) SST in the Pliocene or lower (circle). **(b)** The difference between PlioMIP1 and PlioMIP2 SST. The shape of the symbols at PRISM4 locations indicates whether PlioMIP2 agrees better with proxy data (triangle) or whether PlioMIP1 agrees better (circle).

matches between Eoi^{400} and proxy-derived SSTs at low and high latitudes are of the opposite sign, and data in both regions cannot be simultaneously reconciled simply by changing the CO_2 value. From a global perspective, a value below 400 ppm leads to a better overall fit with PRISM3 data. However, the warming at many of the newer PRISM4 proxy data sites is too high to be reconciled with model data, even at higher CO_2 levels. In the tropical Pacific, more recent reconstructions suggest that Eoi^{400} does not overestimate the SST, as implied by PRISM3 data, thus reducing the global discrepancy. These results underscore firstly, the difficulties in assessing model results with proxy evidence because of different regional discrepancies and uncertainties in proxy estimates and, secondly, a continuing requirement for additional proxy estimates.

Our experiments have not included dynamical vegetation, but previous research employing the same model coupled to a dynamic global vegetation model has shown that such vegetation feedback can amplify both warming in the mid-Holocene (O'ishi and Abe-Ouchi, 2011) and cooling in the cold climate of the LGM (O'ishi and Abe-Ouchi, 2013), especially at northern high latitudes. Subsequent Pliocene-related MIROC4m climate simulations will include a configuration with dynamical vegetation. Other recent studies have incorporated the effects of orbital forcing in simulations of the mPWP, with modelled climate, ice sheets and vegetation exhibiting strong regional variations associated with orbital

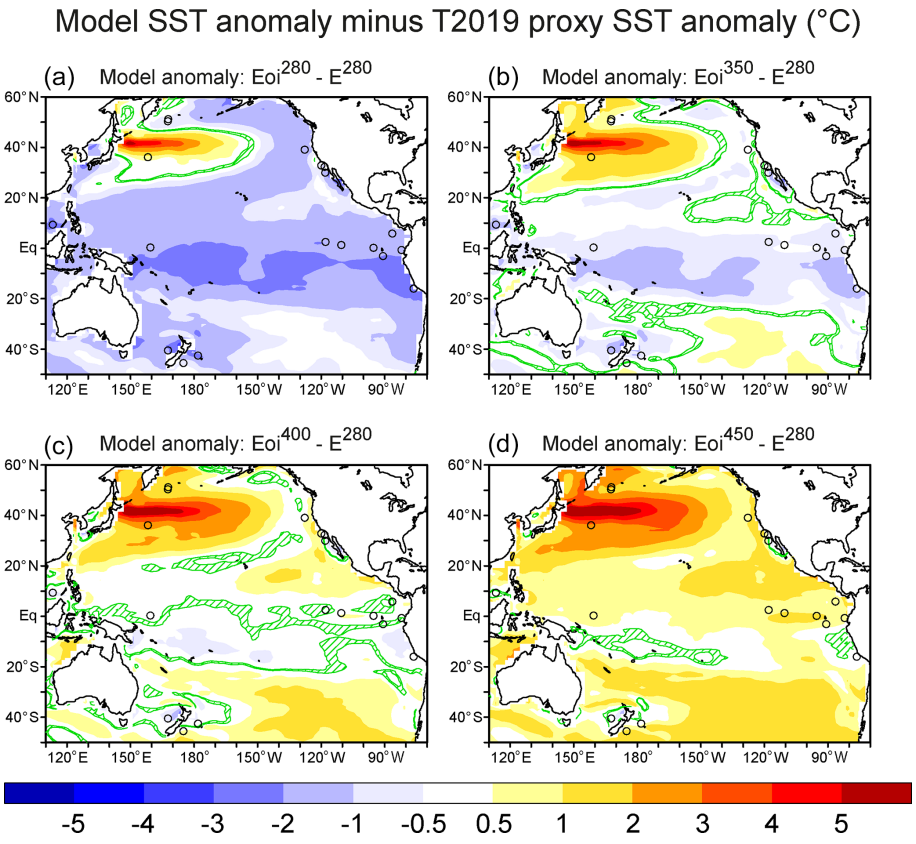

Figure 18. Comparison of annual mean model SST anomalies and T2019 (Tierney et al., 2019) proxy data SST anomalies. Model anomalies refer to the Pliocene experiments, **(a)** Eoi^{280}, **(b)** Eoi^{350}, **(c)** Eoi^{400} and **(d)** Eoi^{450}. For reference, the location of T2019 core sites are shown as black circles. 95 % confidence levels are shown by the green striped area.

parameters, whether as time-dependent forcing in transient simulations (Willeit et al., 2013) or fixed to minimum or maximum forcings (Dolan et al., 2011; Feng et al., 2017). While using present-day orbital parameters for the KM5c interglacial peak appears valid, at least with fixed vegetation (Hunter et al., 2019), an investigation of the mPWP as a whole necessitates more realistic orbital parameters, even when restricted to interglacial peaks (Prescott et al., 2018). This should be borne in mind when considering paleoclimate modelling experiments such as those for the mPWP.

Data availability. Data files containing the PlioMIP2 boundary conditions are directly accessible from the USGS PlioMIP2 website: https://geology.er.usgs.gov/egpsc/prism/7_pliomip2.html (Dowsett, 2020). Data for most experiments in this study are available on the PlioMIP2 data repository at the University of Leeds: ftp://see-gw-01.leeds.ac.uk (Haywood, 2020). Request for access should be directed to Alan M. Haywood. For all other data, readers are asked to contact the lead author, Wing-Le Chan (wlchan@aori.u-tokyo.ac.jp).

Supplement. The supplement related to this article is available online at: https://doi.org/10.5194/cp-16-1523-2020-supplement.

Author contributions. Both authors contributed to the writing of the paper and discussions. WLC set up and carried out the experiments, wrote the first draft of the paper, and prepared all the figures.

Competing interests. The authors declare that they have no conflict of interest.

Special issue statement. This article is part of the special issue "PlioMIP Phase 2: experimental design, implementation and scientific results". It is not associated with a conference.

Acknowledgements. The authors acknowledge JAMSTEC for use of the Earth Simulator supercomputer. This paper benefitted greatly from the comments of two anonymous reviewers. The authors would like to thank them and the editor, Aisling Dolan.

Financial support. This research has been supported by the JSPS Kakenhi (Japan) (grant no. 17H06104) and the MEXT Kakenhi (Japan) (grant no. 17H06323).

Review statement. This paper was edited by Aisling Dolan and reviewed by two anonymous referees.

References

Bakker, P., Schmittner, A., Lenaerts, J. T. M., Abe-Ouchi, A., Bi, D., van den Broeke, M. R., Chan, W.-L., Hu, A., Beadling, R. L., Marsland, S. J., Mernild, S. H., Saenko, O. A., Swingedouw, D., Sullivan, A., and Yin, Y.: Fate of the Atlantic Meridional Overturning Circulation: Strong decline under continued warming and Greenland melting, Geophys. Res. Lett., 43, 12252–12260 https://doi.org/10.1002/2016GL070457, 2016.

Bartoli, G., Hönisch, B., and Zeebe, R. E.: Atmospheric CO_2 decline during the Pliocene intensification of Northern Hemisphere glaciations, Paleoceanography, 26, PA4213, https://doi.org/10.1029/2010PA002055, 2011.

Braconnot, P., Otto-Bliesner, B., Harrison, S., Joussaume, S., Peterchmitt, J.-Y., Abe-Ouchi, A., Crucifix, M., Driesschaert, E., Fichefet, Th., Hewitt, C. D., Kageyama, M., Kitoh, A., Laîné, A., Loutre, M.-F., Marti, O., Merkel, U., Ramstein, G., Valdes, P., Weber, S. L., Yu, Y., and Zhao, Y.: Results of PMIP2 coupled simulations of the Mid-Holocene and Last Glacial Maximum – Part 1: experiments and large-scale features, Clim. Past, 3, 261–277, https://doi.org/10.5194/cp-3-261-2007, 2007.

Bragg, F. J., Lunt, D. J., and Haywood, A. M.: Mid-Pliocene climate modelled using the UK Hadley Centre Model: PlioMIP Experiments 1 and 2, Geosci. Model Dev., 5, 1109–1125, https://doi.org/10.5194/gmd-5-1109-2012, 2012.

Brigham-Grette, J., Melles, M., Minyuk, P., Andreev, A., Tarasov, P., DeConto, R., Koenig, S., Nowaczyk, N., Wennrich, V., Rosén, P., Haltia, E., Cook, T., Gebhardt, C., Meyer-Jacob, C., Snyder, J., and Herzschuh, U.: Pliocene Warmth, Polar Amplification, and Stepped Pleistocene Cooling Recorded in NE Arctic Russia, Science, 340, 1421–1427, https://doi.org/10.1126/science.1233137, 2013.

Burke, K. D., Williams, J. W., Chandler, M. A., Haywood, A. M., Lunt, D. J., and Otto-Bliesner, B. L.: Pliocene and Eocene provide best analogs for near-future climates, Proc. Natl., Acad. Sci. USA, 115, 13288–13293, https://doi.org/10.5061/dryad.0j18k00, 2018.

Chan, W.-L., Abe-Ouchi, A., and Ohgaito, R.: Simulating the mid-Pliocene climate with the MIROC general circulation model: experimental design and initial results, Geosci. Model Dev., 4, 1035–1049, https://doi.org/10.5194/gmd-4-1035-2011, 2011.

Chandan, D. and Peltier, W. R.: Regional and global climate for the mid-Pliocene using the University of Toronto version of CCSM4 and PlioMIP2 boundary conditions, Clim. Past, 13, 919–942, https://doi.org/10.5194/cp-13-919-2017, 2017.

Chandan, D. and Peltier, W. R.: On the mechanisms of warming the mid-Pliocene and the inference of a hierarchy of climate sensitivities with relevance to the understanding of climate futures, Clim. Past, 14, 825–856, https://doi.org/10.5194/cp-14-825-2018, 2018.

Chandler, M. A., Rind, D., and Thompson, R.: Joint investigations of the middle Pliocene II: GISS GCM Northern Hemisphere results, Global Planet. Change, 9, 197–219, https://doi.org/10.1016/0921-8181(94)90016-7, 1994.

Chandler, M., Dowsett, H., and Haywood, A.: The PRISM Model/Data Cooperative: Mid-Pliocene data–model comparisons, PAGES News, 16, 24–25, 2008.

Crampton-Flood, E. M., Peterse, F., Munsterman, D., and Sinninghe Damsté, J. S.: Using tetraether lipids archived in North Sea Basin sediments to extract North Western European Pliocene continental air temperatures, Earth Planet. Sci. Lett., 490, 193–205, https://doi.org/10.1016/j.epsl.2018.03.030, 2018.

Dolan, A. M., Haywood, A. M., Hill, D. J., Dowsett, H. J., Hunter, S. J., Lunt, D. J., and Pickering, S. J.: Sensitivity of Pliocene ice sheets to orbital forcing, Palaeogeogr. Palaeocl., 309, 98–110, https://doi.org/10.1016/j.palaeo.2011.03.030, 2011.

Dowsett, H.: Pliocene Model Intercomparison Project, Phase 2, available at: https://geology.er.usgs.gov/egpsc/prism/7_pliomip2.html, last access: 10 August 2020.

Dowsett, H., Thompson, R., Barron, J., Cronin, T., Fleming, F., Ishman, S., Poore, R., Willard, D., and Holtz Jr., T.: Joint investigations of the Middle Pliocene climate I: PRISM paleoenvironmental reconstructions, Glob. Planet. Change, 9, 169–195, https://doi.org/10.1016/0921-8181(94)90015-9, 1994.

Dowsett, H. J., Barron, J. A., Poore, R. Z., Thompson, R. S., Cronin, T. M., Ishman, S. E., and Willard, D. A.: Middle Pliocene paleoenvironmental reconstruction: PRISM2, US Geol. Surv., Open File Rep. 99-535, 23 pp., 1999.

Dowsett, H. J., Foley, K. M., Stoll, D. K., Chandler, M. A., Sohl, L. E., Bentsen, M., Otto-Bliesner, B. L., Bragg, F. J., Chan, W.-L., Contoux, C., Dolan, A. M., Haywood, A. M., Jonas, J. A., Jost, A., Kamae, Y., Lohmann, G., Lunt, D. J., Nisancioglu, K. H., Abe-Ouchi, A., Ramstein, G., Riesselman, C. R., Robinson, M. M., Rosenbloom, N. A., Salzmann, U., Stepanek, C., Strother, S. L., Ueda, H., Yan, Q., and Zhang, Z.: Sea Surface Temperature of the mid-Piacenzian Ocean: A Data-Model Comparison. Sci. Rep.-UK, 3, 1–8, https://doi.org/10.1038/srep02013, 2013.

Dowsett, H., Dolan, A., Rowley, D., Moucha, R., Forte, A. M., Mitrovica, J. X., Pound, M., Salzmann, U., Robinson, M., Chandler, M., Foley, K., and Haywood, A.: The PRISM4 (mid-Piacenzian) paleoenvironmental reconstruction, Clim. Past, 12, 1519–1538, https://doi.org/10.5194/cp-12-1519-2016, 2016.

Fedorov, A. V., Brierley, C. M., Lawrence, K. T., Liu, Z., Dekens, P. S., and Ravelo, A. C.: Patterns and mechanisms of early Pliocene warmth, Nature, 496, 43–49, https://doi.org/10.1038/nature12003, 2013.

Feng, R., Otto-Bliesner, B. L., Fletcher, T. L., Tabor, C. R., Ballantyne, A. P., and Brady, E. C.: Amplified Late Pliocene terrestrial warmth in northern high latitudes from greater radiative forcing and closed Arctic Ocean gateways, Earth Planet. Sci. Lett., 466, 129–138, https://doi.org/10.1016/j.epsl.2017.03.006, 2017.

Feng, R., Otto-Bliesner, B. L., Brady, E. C., and Rosenbloom, N. A.: Increased Climate Response and Earth System Sensitivity from CCSM4 to CESM2 in mid-Pliocene simulations, J. Adv. Model. Earth Syst., 12, https://doi.org/10.1029/2019MS002033, 2020.

Fletcher, T., Feng, R., Telka, A. M., Matthews Jr, J. V., and Ballantyne, A.: Floral Dissimilarity and the Influence of Climate in the Pliocene High Arctic: Biotic and Abiotic Influences on Five Sites

on the Canadian Arctic Archipelago, Front. Ecol. Evol. 5, 1–13, https://doi.org/10.3389/fevo.2017.00019, 2017.

Foley, K. M. and Dowsett, H. J.: Community sourced mid-Piacenzian sea surface temperature (SST) data, US Geological Survey data release, https://doi.org/10.5066/P9YP3DTV, 2019.

Haywood, A. M.: PlioMIP2 data repository, available at: ftp://see-gw-01.leeds.ac.uk, last access: 10 August 2020.

Haywood, A. M. and Valdes, P. J.: Modelling Pliocene warmth: contribution of atmosphere, oceans and cryosphere, Earth Planet. Sci. Lett., 218, 363–377, https://doi.org/10.1016/S0012-821X(03)00685-X, 2004.

Haywood, A. M., Dowsett, H. J., Otto-Bliesner, B., Chandler, M. A., Dolan, A. M., Hill, D. J., Lunt, D. J., Robinson, M. M., Rosenbloom, N., Salzmann, U., and Sohl, L. E.: Pliocene Model Intercomparison Project (PlioMIP): experimental design and boundary conditions (Experiment 1), Geosci. Model Dev., 3, 227–242, https://doi.org/10.5194/gmd-3-227-2010, 2010.

Haywood, A. M., Dowsett, H. J., Robinson, M. M., Stoll, D. K., Dolan, A. M., Lunt, D. J., Otto-Bliesner, B., and Chandler, M. A.: Pliocene Model Intercomparison Project (PlioMIP): experimental design and boundary conditions (Experiment 2), Geosci. Model Dev., 4, 571–577, https://doi.org/10.5194/gmd-4-571-2011, 2011.

Haywood, A. M., Dowsett, H. J., Dolan, A. M., Rowley, D., Abe-Ouchi, A., Otto-Bliesner, B., Chandler, M. A., Hunter, S. J., Lunt, D. J., Pound, M., and Salzmann, U.: The Pliocene Model Intercomparison Project (PlioMIP) Phase 2: scientific objectives and experimental design, Clim. Past, 12, 663–675, https://doi.org/10.5194/cp-12-663-2016, 2016.

Haywood, A. M., Hill, D. J., Dolan, A. M., Otto-Bliesner, B. L., Bragg, F., Chan, W.-L., Chandler, M. A., Contoux, C., Dowsett, H. J., Jost, A., Kamae, Y., Lohmann, G., Lunt, D. J., Abe-Ouchi, A., Pickering, S. J., Ramstein, G., Rosenbloom, N. A., Salzmann, U., Sohl, L., Stepanek, C., Ueda, H., Yan, Q., and Zhang, Z.: Large-scale features of Pliocene climate: results from the Pliocene Model Intercomparison Project, Clim. Past, 9, 191–209, https://doi.org/10.5194/cp-9-191-2013, 2013.

Haywood, A. M., Tindall, J. C., Dowsett, H. J., Dolan, A. M., Foley, K. M., Hunter, S. J., Hill, D. J., Chan, W.-L., Abe-Ouchi, A., Stepanek, C., Lohmann, G., Chandan, D., Peltier, W. R., Tan, N., Contoux, C., Ramstein, G., Li, X., Zhang, Z., Guo, C., Nisancioglu, K. H., Zhang, Q., Li, Q., Kamae, Y., Chandler, M. A., Sohl, L. E., Otto-Bliesner, B. L., Feng, R., Brady, E. C., von der Heydt, A. S., Baatsen, M. L. J., and Lunt, D. J.: A return to large-scale features of Pliocene climate: the Pliocene Model Intercomparison Project Phase 2, Clim. Past Discuss., https://doi.org/10.5194/cp-2019-145, in review, 2020.

Hill, D. J., Haywood, A. M., Lunt, D. J., Hunter, S. J., Bragg, F. J., Contoux, C., Stepanek, C., Sohl, L., Rosenbloom, N. A., Chan, W.-L., Kamae, Y., Zhang, Z., Abe-Ouchi, A., Chandler, M. A., Jost, A., Lohmann, G., Otto-Bliesner, B. L., Ramstein, G., and Ueda, H.: Evaluating the dominant components of warming in Pliocene climate simulations, Clim. Past, 10, 79–90, https://doi.org/10.5194/cp-10-79-2014, 2014.

Hunter, S. J., Haywood, A. M., Dolan, A. M., and Tindall, J. C.: The HadCM3 contribution to PlioMIP phase 2, Clim. Past, 15, 1691–1713, https://doi.org/10.5194/cp-15-1691-2019, 2019.

IPCC: Climate Change 2013: The Physical Science Basis. Contribution of Working Group I of the Fifth Assessment Report of the Intergovernmental Panel on Climate Change, edited by: Stocker, T. F., Qin, D., Plattner, G.-K., Tignor, M., Allen, S. K., Boschung, J., Nauels, A., Xia, Y., Bex, V., and Midgley, P. M., Cambridge, UK, 1585 pp., 2013.

Jochum, M., Fox-Kemper, B., Molnar, P. H., and Shields, C.: Differences in the Indonesian seaway in a coupled climate model and their relevance to Pliocene climate and El Niño, Paleoceanography, 24, PA1212, https://doi.org/10.1029/2008PA001678, 2009.

K-1 model developers: K-1 coupled model (MIROC) description. K-1 technical report, edited by: Hasumi, H. and Emori, S., Center for Climate System Research, The University of Tokyo, Japan, 34 pp., available at: https://ccsr.aori.u-tokyo.ac.jp/~hasumi/miroc_description.pdf (last access: 10 August 2020), 2004.

Kamae, Y., Yoshida, K., and Ueda, H.: Sensitivity of Pliocene climate simulations in MRI-CGCM2.3 to respective boundary conditions, Clim. Past, 12, 1619–1634, https://doi.org/10.5194/cp-12-1619-2016, 2016.

Hasumi, H.: CCSR Ocean Component Model (COCO) Version 2.1, CCSR Report, The University of Tokyo, Japan, 13, 65 pp., 2000.

Kageyama, M., Braconnot, P., Harrison, S. P., Haywood, A. M., Jungclaus, J. H., Otto-Bliesner, B. L., Peterschmitt, J.-Y., Abe-Ouchi, A., Albani, S., Bartlein, P. J., Brierley, C., Crucifix, M., Dolan, A., Fernandez-Donado, L., Fischer, H., Hopcroft, P. O., Ivanovic, R. F., Lambert, F., Lunt, D. J., Mahowald, N. M., Peltier, W. R., Phipps, S. J., Roche, D. M., Schmidt, G. A., Tarasov, L., Valdes, P. J., Zhang, Q., and Zhou, T.: The PMIP4 contribution to CMIP6 – Part 1: Overview and overarching analysis plan, Geosci. Model Dev., 11, 1033–1057, https://doi.org/10.5194/gmd-11-1033-2018, 2018.

Kürschner, W. M., van der Burgh, J., Visscher, H., and Dilcher, D. L.: Oak leaves as biosensors of late Neogene and early Pleistocene paleoatmospheric CO_2 concentrations, Mar. Micropaleontol., 27, 299–312, https://doi.org/10.1016/0377-8398(95)00067-4, 1996.

Le Trent, H. and Li, Z.-X.: Sensitivity of an atmospheric general circulation model to prescribed SST changes: feedback effects associated with the simulation of cloud optical properties, Clim. Dynam., 5, 175–187, https://doi.org/10.1007/BF00251808, 1991.

Li, X., Guo, C., Zhang, Z., Otterå, O. H., and Zhang, R.: PlioMIP2 simulations with NorESM-L and NorESM1-F, Clim. Past, 16, 183–197, https://doi.org/10.5194/cp-16-183-2020, 2020.

Lunt, D. J., Valdes, P. J., Haywood, A. M., and Rutt, I. C.: Closure of the Panama Seaway during the Pliocene: implications for climate and Northern Hemisphere glaciation, Clim. Dyn., 30, 1–18, https://doi.org/10.1007/s00382-007-0265-6, 2008.

Lunt, D. J., Haywood, A. M., Schmidt, G. A., Salzmann, U., Valdes, P. J., and Dowsett, H. J.: Earth system sensitivity inferred from Pliocene modelling and data, Nature Geosci., 3, 60–64, https://doi.org/10.1038/NGEO706, 2010.

Martínez-Botí, M. A., Foster, G. L., Chalk, T. B., Rohling, E. J., Sexton, P. F., Lunt, D. J., Pancost, R. D., Badger, M. P. S., and Schmidt, D. N.: Plio-Pleistocene climate sensitivity evaluated using high-resolution CO_2 records, Nature, 518, 49–54, https://doi.org/10.1038/nature14145, 2015.

Mellor, G. L. and Yamada, T.: Development of a turbulence closure model for geostrophic fluid problems, Rev. Geophys., 20, 851–875, https://doi.org/10.1029/RG020i004p00851, 1982.

Nakajima, T., Tsukamoto, M., Tsushima, Y., Numaguti, A., and Kimura, T.: Modelling of the radiative process in an atmospheric general circulation model, Appl. Opt., 39, 4869–4878, https://doi.org/10.1364/AO.39.004869, 2000.

Noh, Y. and Kim, H.-J.: Simulations of temperature and turbulence structure of the oceanic boundary layer with the improved near-surface process, J. Geophys. Res., 104, 15621–15634, https://doi.org/10.1029/1999JC900068, 1999.

Numaguti, A., Takahashi, M., Nakajima, T., and Sumi, A.: Description of CCSR/NIES Atmospheric General Circulation Model, CGERs Supercomputer Monograph Report, Center for Global Environment Research, National Institute for Environmental Studies, 3, 1–48, 1997.

Obase, T. and Abe-Ouchi, A.: Abrupt Bølling-Allerød Warming Simulated under Gradual Forcing of the Last Deglaciation, Geophys. Res. Lett., 46, 11397–11405, https://doi.org/10.1029/2019GL084675, 2019.

Ohgaito, R., Sueyoshi, T., Abe-Ouchi, A., Hajima, T., Watanabe, S., Kim, H.-J., Yamamoto, A., and Kawamiya, M.: Can an Earth System Model simulate better climate change at mid-Holocene than an AOGCM? A comparison study of MIROC-ESM and MIROC3, Clim. Past, 9, 1519–1542, https://doi.org/10.5194/cp-9-1519-2013, 2013.

O'ishi, R. and Abe-Ouchi, A: Polar amplification in the mid-Holocene derived from dynamical vegetation change with a GCM, Geophys. Res. Lett., 38, L14702, https://doi.org/10.1029/2011GL048001, 2011.

O'ishi, R. and Abe-Ouchi, A.: Influence of dynamic vegetation on climate change and terrestrial carbon storage in the Last Glacial Maximum, Clim. Past, 9, 1571–1587, https://doi.org/10.5194/cp-9-1571-2013, 2013.

Oka, A., Hasumi, H., Okada, N., Sakamoto, T. T., and Suzuki, T.: Deep convection seesaw controlled by freshwater transport through the Denmark Strait, Ocean Modell., 15, 157–176, https://doi.org/10.1016/j.ocemod.2006.08.004, 2006.

Otto-Bliesner, B. L., Jahn, A. Feng, R. Brady, E. C., Hu, A., and Löfverström, M.: Amplified North Atlantic warming in the late Pliocene by changes in Arctic gateways, Geophys. Res. Lett., 44, 957–964, https://doi.org/10.1002/2016GL071805, 2017.

Panitz, S., Salzmann, U., Risebrobakken, B., De Schepper, S., and Pound, M. J.: Climate variability and long-term expansion of peatlands in Arctic Norway during the late Pliocene (ODP Site 642, Norwegian Sea), Clim. Past, 12, 1043–1060, https://doi.org/10.5194/cp-12-1043-2016, 2016.

Prescott, C. L., Dolan, A. M., Haywood, A. M., Hunter, S. J., and Tindall, J. C.: Regional climate and vegetation response to orbital forcing within the mid-Pliocene Warm Period: A study using HadCM3, Global Planet. Change, 161, 231–243, https://doi.org/10.1016/j.gloplacha.2017.12.015, 2018.

Raymo, M., Grant, B., Horowitz, M., and Rau, G.: Mid-Pliocene warmth: stronger greenhouse and stronger conveyor, Mar. Micropaleontol. 27, 313–326, https://doi.org/10.1016/0377-8398(95)00048-8, 1996.

Salzmann, U., Haywood, A. M., Lunt D. J., Valdes, P. J., and Hill, D. J.: A new global biome reconstruction and data-model comparison for the Middle Pliocene, Global Ecol. Biogeogr., 17, 432–447, https://doi.org/10.1111/j.1466-8238.2008.00381.x, 2008.

Salzmann, U., Dolan, A. M., Haywood, A. M., Chan, W.-L., Voss, J., Hill, D. J., Abe-Ouchi, A., Otto-Bliesner, B. L., Bragg, F. J., Chandler, M. A., Contoux, C., Dowsett, H. J., Jost, A., Kamae, Y., Lohmann, G., Lunt, D. J., Pickering, S. J., Pound, M. J., Ramstein, G., Rosenbloom, N. A., Sohl, L. E., Stepanek, C., Ueda, H., and Zhang, Z.: Challenges in quantifying Pliocene terrestrial warming revealed by data–model discord, Nature Clim. Change, 3, 969–974, https://doi.org/10.1038/nclimate2008, 2013.

Samakinwa, E., Stepanek, C., and Lohmann, G.: Sensitivity of mid-Pliocene climate to changes in orbital forcing, and PlioMIP's boundary conditions, Clim. Past Discuss., https://doi.org/10.5194/cp-2020-5, in review, 2020.

Seki, O., Foster, G. L., Schmidt, D. N., Mackensen, A., Kawamura, K., and Pancost, R. D.: Alkenone and boron-based Pliocene pCO_2 records, Earth Planet. Sci. Lett. 292, 201–211, https://doi.org/10.1016/j.epsl.2010.01.037, 2010.

Sévellec, F. and Fedorov, A. V.: AMOC sensitivity to surface buoyancy fluxes: Stronger ocean meridional heat transport with a weaker volume transport?, Clim. Dynam., 47, 1497–1513, https://doi.org/10.1007/s00382-015-2915-4, 2016.

Sherriff-Tadano, S. and Abe-Ouchi, A.: Roles of sea ice–surface wind feedback in maintaining the glacial Atlantic meridional overturning circulation and climate, J. Clim., 33, 3001–3018, https://doi.org/10.1175/JCLI-D-19-0431.1, 2020.

Sloan, L. C., Crowley, T. J., and Pollard, D.: Modeling of middle Pliocene climate with the NCAR GENESIS general circulation model, Mar. Micropaleontol., 27, 51–61, https://doi.org/10.1016/0377-8398(95)00063-1, 1996.

Takata, K., Watanabe, T., and Emori, S.: Development of the minimal advanced treatments of surface interaction and runoff, Global Planet. Change, 38, 209–222, https://doi.org/10.1016/S0921-8181(03)00030-4, 2003.

Takemura, T., Okamoto, H., Maruyama, Y., Numaguti, A., Higurashi, A., and Nakajima, T.: Global three-dimensional simulation of aerosol optical thickness distribution of various origins, J. Geophys. Res., 105, 17853–17873, https://doi.org/10.1029/2000JD900265, 2000.

Tan, N., Contoux, C., Ramstein, G., Sun, Y., Dumas, C., Sepulchre, P., and Guo, Z.: Modeling a modern-like pCO_2 warm period (Marine Isotope Stage KM5c) with two versions of an Institut Pierre Simon Laplace atmosphere–ocean coupled general circulation model, Clim. Past, 16, 1–16, https://doi.org/10.5194/cp-16-1-2020, 2020.

Tierney, J. E., Haywood, A. M., Feng, R., Bhattacharya, T., and Otto-Bliesner, B. L.: Pliocene Warmth Consistent With Greenhouse Gas Forcing, Geophys. Res. Lett., 46, 9136–9144, https://doi.org/10.1029/2019GL083802, 2019.

Tripati, A. K., Roberts, C. D., and Eagle, R. A.: Coupling of CO_2 and ice sheet stability over major climate transitions of the last 20 million years, Science, 326, 1394–1397, https://doi.org/10.1126/science.1178296, 2009.

Willeit, M., Ganopolski, A., and Feulner, G.: On the effect of orbital forcing on mid-Pliocene climate, vegetation and ice sheets, Clim. Past, 9, 1749–1759, https://doi.org/10.5194/cp-9-1749-2013, 2013.

Yanase, W. and Abe-Ouchi, A.: The LGM surface climate and atmospheric circulation over East Asia and the North Pacific in the PMIP2 coupled model simulations, Clim. Past, 3, 439–451, https://doi.org/10.5194/cp-3-439-2007, 2007.

Zhang, R., Yan, Q., Zhang, Z. S., Jiang, D., Otto-Bliesner, B. L., Haywood, A. M., Hill, D. J., Dolan, A. M., Stepanek, C.,

Lohmann, G., Contoux, C., Bragg, F., Chan, W.-L., Chandler, M. A., Jost, A., Kamae, Y., Abe-Ouchi, A., Ramstein, G., Rosenbloom, N. A., Sohl, L., and Ueda, H.: Mid-Pliocene East Asian monsoon climate simulated in the PlioMIP, Clim. Past, 9, 2085–2099, https://doi.org/10.5194/cp-9-2085-2013, 2013.

Zhang, Z.-S., Nisancioglu, K. H., Chandler, M. A., Haywood, A. M., Otto-Bliesner, B. L., Ramstein, G., Stepanek, C., Abe-Ouchi, A., Chan, W.-L., Bragg, F. J., Contoux, C., Dolan, A. M., Hill, D. J., Jost, A., Kamae, Y., Lohmann, G., Lunt, D. J., Rosenbloom, N. A., Sohl, L. E., and Ueda, H.: Mid-pliocene Atlantic Meridional Overturning Circulation not unlike modern, Clim. Past, 9, 1495–1504, https://doi.org/10.5194/cp-9-1495-2013, 2013.

Zheng, J., Zhang, Q., Li, Q., Zhang, Q., and Cai, M.: Contribution of sea ice albedo and insulation effects to Arctic amplification in the EC-Earth Pliocene simulation, Clim. Past, 15, 291–305, https://doi.org/10.5194/cp-15-291-2019, 2019.